

Physical Interpretation of the Angle Dependent Magnetic Helicity Spectrum in the Solar Wind: The Nature of Turbulent Fluctuations near the Proton Gyroradius Scale

Kristopher G. Klein, Gregory G. Howes

Department of Physics and Astronomy, University of Iowa, Iowa City, Iowa 52242, USA.

kristopher-klein@uiowa.edu

and

Jason M. TenBarge

IREAP, University of Maryland, College Park, Maryland 20742, USA.

and

John J. Podesta

Center for Space Plasma Physics, Space Science Institute, Boulder, CO 80301

ABSTRACT

Motivated by recent observations of distinct parallel and perpendicular signatures in magnetic helicity measurements segregated by wave period and angle between the local magnetic field and the solar wind velocity, this paper undertakes a comparison of three intervals of *Ulysses* data with synthetic time series generated from a physically motivated turbulence model. From these comparisons, it is hypothesized that the observed signatures result from a perpendicular cascade of Alfvénic fluctuations and a local, non-turbulent population of ion cyclotron or whistler waves generated by temperature anisotropy instabilities. By constraining the model’s free parameters through comparison to *in situ* data, it is found that, on average, $\sim 95\%$ of the power near dissipative scales is contained in a perpendicular Alfvénic cascade and that the parallel fluctuations are propagating nearly unidirectionally. The effects of aliasing on magnetic helicity measurements are considered and shown to be significant near the Nyquist frequency.

1. Introduction

Turbulence is ubiquitous in space and astrophysical plasmas. In the heliosphere, it plays a critical role in plasma heating and the scattering of cosmic rays and energetic solar particles. Given the availability of detailed *in situ* measurements from a broad range of heliophysics missions, the near-Earth solar wind is an ideal environment in which to study the fundamental nature of plasma turbulence. In the solar wind, the primary focus is the transport of energy from large scale turbulent motions to the small length scales at which the turbulence may be dissipated and the energy ultimately converted to plasma heat. Key questions

at the forefront of solar wind turbulence investigations are: (i) what are the characteristics of the turbulent fluctuations?; (ii) what are the properties of the nonlinear interactions that drive the turbulent cascade of energy?; and (iii) what are the physical dissipation mechanisms that damp the turbulence and ultimately lead to plasma heating? The answers to each of these questions are interdependent. In particular, the nature of the electromagnetic and plasma fluctuations underlying the turbulence constrains the possible dissipation mechanisms.

The definitive determination of the characteristics of the turbulent fluctuations, however, is made difficult due to the fact that the bulk of current

in situ solar wind observations are single point measurements. The Taylor hypothesis (Taylor 1938) is typically invoked, because of the super-Alfvénic velocity of the solar wind near 1 AU, to transform from the observed frequency of the advected turbulent fluctuations to a length scale of the fluctuations. For low frequency fluctuations with $\omega \lesssim \Omega_i$ and with the exception of a small number of studies of solar wind turbulence employing analyses based on multi-spacecraft measurements, we have no knowledge of the frequency of the fluctuations in the rest frame of the solar wind plasma. This limitation drives the quest to exploit alternative means to illuminate the character of the turbulent fluctuations in the solar wind. A wide range of characteristics, including polarizations, helicities, and other transport ratios have previously been used to decipher the dynamics of space plasmas (Song et al. 1994; Gary & Winske 1992; Lacombe & Belmont 1995). Here we employ the magnetic helicity as a sensitive probe for turbulent fluctuations in the solar wind.

The *fluctuating magnetic helicity*, defined as $H'_m \equiv \int d^3\mathbf{r} \delta\mathbf{A} \cdot \delta\mathbf{B}$, where $\delta\mathbf{A}$ and $\delta\mathbf{B}$ are respectively the fluctuations of the vector potential and magnetic field, was first proposed as a useful metric for studying turbulent fluctuations in the solar wind by Matthaeus & Goldstein (1982). The *reduced fluctuating magnetic helicity*, $H_m^{r'}$ (Matthaeus et al. 1982), is related to H'_m but is derivable from single-point spacecraft measurements and is a function of spacecraft-frame frequency ω_{SC} , (Howes & Quataert 2010):

$$H_m^{r'}(\omega_{SC}) = \sum_{\mathbf{k}} \frac{i[\mathbf{B}_2(\mathbf{k})\mathbf{B}_3^*(\mathbf{k}) - \mathbf{B}_2^*(\mathbf{k})\mathbf{B}_3(\mathbf{k})]}{\omega_{SC}/V_{SW}} \times \delta[\omega_{SC} - (\mathbf{k} \cdot \mathbf{V}_{SW} + \omega)], \quad (1)$$

where \mathbf{V}_{SW} is the solar wind velocity. Normalizing $H_m^{r'}$ by the trace power $|\mathbf{B}(k_1)|^2$ yields the *normalized reduced fluctuating magnetic helicity*, $\sigma'_m = k_1 H_m^{r'}(k_1)/|\mathbf{B}(k_1)|^2$, where $k_1 \equiv \omega_{SC}/V_{SW}$ is the projection of the wavevector along the direction of the solar wind. The normalized reduced fluctuating magnetic helicity is bound between -1 and 1 . For simplicity, throughout this paper the simplified term “magnetic helicity” is used instead of the more cumbersome “normalized reduced fluctuating magnetic helicity”.

Spacecraft measurements of σ'_m in the near-Earth solar wind at low spacecraft-frame frequen-

cies, $f \ll 1$ Hz, typically give values that fluctuate about zero, which was originally interpreted as an admixture of waves with left-handed ($\sigma'_m \simeq -1$) and right-handed ($\sigma'_m \simeq +1$) magnetic helicities (Matthaeus et al. 1982). Based on the eigenfunctions of the linear Vlasov-Maxwell dispersion relation, Gary (1986) later showed that, at large-scales $k\rho_i \ll 1$, the linear waves have very small intrinsic magnetic helicity, $\sigma'_m \simeq 0$, which eliminated the need for an explanation in terms of a mixture of waves with left- and right-handed helicities. At higher spacecraft-frame frequencies, $f \sim 1$ Hz, *in situ* measurements of the magnetic field fluctuations produced an identifiably nonzero value of σ'_m (Goldstein et al. 1994; Leamon et al. 1998). This was initially interpreted as evidence of the damping of left-hand polarized ion cyclotron waves (ICWs) and the persistence of right-hand polarized whistler waves.

Subsequently, it was shown that an anisotropic turbulent spectrum of Alfvén waves and kinetic Alfvén waves (KAWs) naturally reproduces both the low and high frequency measurements (Howes & Quataert 2010). As KAWs have preferentially perpendicular wavevectors, $k_\perp > k_\parallel$, and ICWs and whistler waves require sufficiently large parallel wavevectors, $k_\parallel d_i \gtrsim 1$, where \perp and \parallel refer to orientation with respect to the *local* mean magnetic field \mathbf{B}_0 , the KAW model has the added benefit of being compatible with the predominantly perpendicular cascade of energy expected from anisotropic magnetized turbulence theories (Goldreich & Sridhar 1995; Boldyrev 2006). Two recent studies (He et al. 2011; Podesta & Gary 2011b), analyzed the magnetic helicity of solar wind fluctuations as a function of the wave period T in the spacecraft frame and the angle θ between the solar wind velocity \mathbf{V}_{SW} and \mathbf{B}_0 , and discovered two distinct signatures at angles perpendicular and parallel to \mathbf{B}_0 at spacecraft-frame frequencies $f \sim 1$ Hz. These observations have been interpreted as two separate populations of fluctuations at kinetic scales with wavevectors oriented parallel and perpendicular to the local mean magnetic field (Podesta & Gary 2011a; He et al. 2012).

We here explore the properties of a model for solar wind turbulence that reproduces the observed behavior of the magnetic helicity. In particular, we show that the properties of the model are tightly constrained by spacecraft observations

of the magnetic helicity plotted as a function of period and angle. This study employs the *synthetic spacecraft data method* (Klein et al. 2012), in which synthetic time series measurements of the magnetic field—measurements that may be directly compared to spacecraft observations—are generated by sampling along a trajectory through the model plasma volume. The turbulent fluctuations in this model are derived from a distribution of linear wave modes with random phases, where the particular distribution of wave power is guided by modern plasma turbulence theory, and where the physical properties of the wave modes are derived from linear kinetic plasma physics. The model’s ability to reproduce the observed magnetic helicity structure is used to constrain the underlying parameters describing the distribution of turbulent wave power, shedding light on the nature of the turbulent fluctuations in the weakly collisional solar wind plasma.

The remainder of the paper is organized as follows. Section 2 provides background on the germane aspects of recent *in situ* magnetic helicity measurements as well as a discussion of the underlying linear kinetic plasma theory. A description of and justification for the underlying turbulence model is given in Section 3. The general method used to generate the synthetic data and the particular results are found in Section 4. Discussion of these results and a conclusion follow in Sections 5 and 6 respectively.

2. Magnetic Helicity

In this section, we review the observations of magnetic helicity in solar wind turbulence and outline the linear kinetic physics that determines the magnetic helicity of each of the characteristic linear wave modes.

2.1. Spacecraft Measurements

Although magnetic helicity has long been used to investigate the nature of turbulent fluctuations in the solar wind (Matthaeus et al. 1982; Matthaeus & Goldstein 1982; Gary 1986; Leamon et al. 1998; Goldstein et al. 1994; Hamilton et al. 2008; Howes & Quataert 2010), only recently has it been shown by plotting the magnetic helicity of the turbulent fluctuations as a function of period and angle that there exist two distinct signatures of the magnetic helicity at scales near

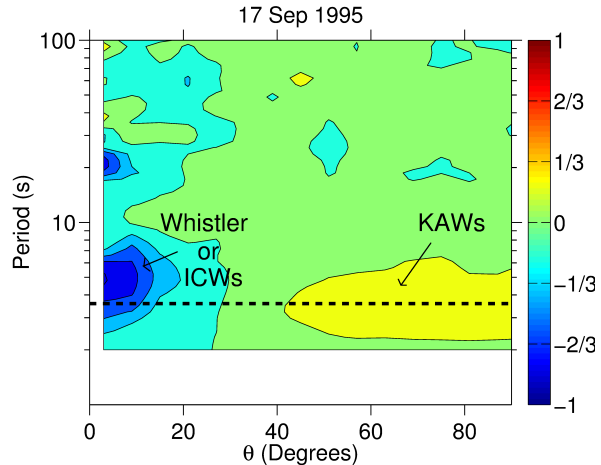


Fig. 1.— Magnetic helicity σ'_m computed from observations by the *Ulysses* spacecraft, plotted as a function of period and angle for interval I. Previous studies have suggested that the perpendicular signature is due to kinetic Alfvén waves (KAWs) and the parallel signature is due to either whistler or ion cyclotron waves (ICWs) (Podesta & Gary 2011b; He et al. 2011). The horizontal dashed line indicates the period approximately corresponding to $k\rho_i = 1$.

$k\rho_i = 1$ (He et al. 2011; Podesta & Gary 2011b). Employing a wavelet analysis of *in situ* magnetic field measurements, both studies calculated σ'_m as a function of the wave period T in the spacecraft frame and the angle θ between the solar wind velocity \mathbf{V}_{SW} and *local* mean magnetic field \mathbf{B}_0 . This method showed that, in a majority of the measurements, there appear two distinct signatures: (i) a broad feature with positive magnetic helicity at large angles centered around $\theta \sim 90^\circ$, and (ii) a more narrow feature with negative magnetic helicity at small angles $\theta \sim 0^\circ$. We denote these distinct features as the *perpendicular* and *parallel signature*, respectively.

These features are clearly visible in Figure 1, a plot of the magnetic helicity σ'_m as a function of period T and angle θ , computed from one of the same *Ulysses* spacecraft data intervals as analyzed by Podesta & Gary (2011b). We note that if the measurements are summed over all angles θ to obtain a frequency spectrum of the magnetic helicity $\sigma'_m(\omega_{SC})$, the signature of the negative magnetic helicity at small angles $\theta \sim 0^\circ$ is com-

pletely masked by the positive helicity at large angles $\theta \sim 90^\circ$ (Podesta & Gary 2011b).

An important difference in the results of He et al. (2011) and Podesta & Gary (2011b) is the magnitude of the maximum value of the parallel magnetic helicity signature. In He et al. (2011), the observed maximum value of $|\sigma_m|$ for the parallel signature is approximately 0.4 while Podesta & Gary (2011b) found a maximum value that is consistently near 1.0. This difference persists even when analyzing essentially the same interval of STEREO data. The different results may be due to subtle differences between the analysis techniques employed in the two studies; further work is needed to identify the cause of these differences. All analysis undertaken and results presented in this study are based upon the observations found in Podesta & Gary (2011b).

Several hypotheses have been proposed to account for the qualitative features of the magnetic helicity plot seen in Figure 1. The perpendicular signature was suggested to arise from an anisotropic distribution of KAWs with $k_\perp \gg k_\parallel$ (He et al. 2011; Podesta & Gary 2011b) or from a spectrum of whistler waves (He et al. 2011). The parallel signature was proposed to arise from ICWs propagating along the magnetic field away from the sun (He et al. 2011; Podesta & Gary 2011b) or whistler waves propagating along the magnetic field toward to the sun (Podesta & Gary 2011b,a). Temperature anisotropy instabilities, such as the electromagnetic ion cyclotron instability and the parallel firehose instability, have been proposed to generate these parallel propagating waves (Podesta & Gary 2011b,a). The maximum growth rate of these instabilities occurs at length scales near the ion inertial length, $k_\parallel d_i \sim 1$ (Podesta & Gary 2011a), as shown in Figure 3, which may explain why the parallel signature is localized near periods $T \sim 5$ s.

In this study, we construct the magnetic helicity plot for three intervals of *Ulysses* data specified in Table 1—intervals that have been previously analyzed in Podesta & Gary (2011b)—for direct comparison to magnetic helicity plots generated by the synthetic spacecraft data method (Klein et al. 2012). A detailed discussion of the *in situ* data analysis techniques can be found in Podesta & Gary (2011b). The first two intervals are from the first northern pass of *Ulysses* while the third is from the southern pass. Contours of

σ'_m from these data sets are presented in the left hand column of Figure 6. The ion plasma beta, $\beta_i \equiv 8\pi n_i T_i / B_0^2$, is $\beta_i \geq 1$ for these three periods, where T_i is the ion temperature in energy units and n_i is the ion density. No interval from the Podesta & Gary (2011b) data set had $\beta_i < 1$. Intervals **I** and **III** both have the parallel and perpendicular signatures as previously described, while interval **II** was chosen as an abnormal period with no visible perpendicular structure. The key question that we ask is, *what do these magnetic helicity measurements tell us about the nature of the turbulent fluctuations in the solar wind?* By making detailed quantitative comparisons to magnetic helicity plots generated by the synthetic spacecraft data method, we hope to illuminate the characteristics of the underlying turbulent fluctuations in the solar wind.

2.2. Linear Kinetic Physics

The kinetic physics of the characteristic plasma waves in a weakly collisional plasma such as the solar wind is used to guide our intuition about the magnetic helicity of turbulent fluctuations. To investigate the linear wave properties in a weakly collisional plasma, we employ the linear Vlasov-Maxwell dispersion relation for a fully ionized proton and electron plasma with isotropic Maxwellian equilibrium distribution functions. The linear Vlasov-Maxwell dispersion relation can be expressed as a function of five dimensionless parameters: $k_\perp \rho_i$, $k_\parallel d_i$, β_i , T_i/T_e , and v_{t_i}/c . Here, $\rho_i = v_{t_i}/\Omega_i$ is the ion Larmor radius, $d_i = c/\omega_{pi} = \rho_i/\sqrt{\beta_i}$ is the ion inertial length, $v_{t_i} = \sqrt{2T_i/m_i}$ is the ion thermal speed (where Boltzmann's constant has been absorbed to express temperature in units of energy), $\Omega_i = eB_0/m_i c$ is the ion cyclotron frequency, $\omega_{pi} = \sqrt{4\pi n_i e^2/m_i}$ is the ion plasma frequency, and c is the speed of light.

The three familiar wave modes in magnetohydrodynamics (MHD)—the Alfvén wave and the fast and slow magnetosonic waves—have kinetic counterparts in a collisionless plasma that, at large scales $k\rho_i \ll 1$, have properties similar to the MHD modes (Klein et al. 2012). Each of these non-dispersive MHD-like waves transitions to a related dispersive wave mode (*e.g.*, kinetic Alfvén waves or whistler waves) at smaller scales corresponding to $k_\perp \rho_i \gtrsim 1$ or $k_\parallel d_i \gtrsim 1$. It has been shown that the compressible energy in the iner-

Interval	Date	β_i	ρ_i/V_{SW} (s)	R (AU)	
I	Sept. 17 14:38 to Sept 18 4:46 1995	1.7	0.544	2.36	1 st Northern Pass
II	May 23 00:32 to 22:20 1995	1.0	0.312	2.36	1 st Northern Pass
III	July 6 22:12 to July 7 05:51 1994.	1.5	0.662	2.76	1 st Southern Pass

Table 1: Selected *Ulysses* data intervals from Podesta & Gary (2011b) chosen for direct comparison to synthetic spacecraft data models.

tial range of turbulence in the solar wind, which constitutes 10% or less of the total turbulent energy at these scales, consists of kinetic slow waves, with a negligible contribution from kinetic fast waves (Howes et al. 2012; Klein et al. 2012). Although this finding merits further investigation of the magnetic helicity of the kinetic slow waves, in this study we focus on the physics of the kinetic fast waves and Alfvén waves and their dispersive extensions at small scales.

The Alfvén wave transitions to the ion cyclotron wave (ICW) in the limit of small parallel scales $k_{\parallel}d_i \gtrsim 1$ and to the kinetic Alfvén wave (KAW) in the anisotropic limit of small perpendicular scales $k_{\perp}\rho_i \gtrsim 1$ and $k_{\perp} \gg k_{\parallel}$. The kinetic fast wave transitions to the whistler wave in the limit of small parallel scales $k_{\parallel}d_i \gtrsim 1$ and to the ion Bernstein wave in the limit of small perpendicular scales $k_{\perp}\rho_i \gtrsim 1$ and $k_{\perp} \gg k_{\parallel}$ (Howes 2009; Verdon et al. 2009). In this study we focus on the magnetic helicity signatures of the kinetic Alfvén wave, ion cyclotron wave, and whistler wave. The regions in the $(k_{\perp}, k_{\parallel})$ plane where these wave modes exist are depicted in Figures 2 and 4.

For an individual plane wave with wavevector \mathbf{k} , we employ the linear Vlasov-Maxwell dispersion relation to determine the eigenfunction of the kinetic fast wave and Alfvén wave and compute the normalized fluctuating magnetic helicity $\sigma_m(\mathbf{k}) \equiv kH'_m(\mathbf{k})/|\mathbf{B}(\mathbf{k})|^2$ as a function of $k_{\perp}\rho_i$ and $k_{\parallel}d_i$, where $H'_m(\mathbf{k})$ is defined in Howes & Quataert (2010). In Figure 2, we plot $\sigma_m(\mathbf{k})$ for the kinetic fast and Alfvén modes for plasma parameters $\beta_i = 1$, $T_i/T_e = 1$, and $v_{t_i}/c = 10^{-4}$. We adopt the convention that $\omega > 0$, so that the wave propagation direction along the magnetic field is determined by the sign of k_{\parallel} . The plot in Figure 2 employs $k_{\parallel} > 0$.

In Figure 2, we show that large scale, isotropic fluctuations of both the kinetic fast (bottom) and Alfvén (top) modes have a magnetic helicity of nearly zero. For nearly parallel wavevectors $k_{\parallel} \gg$

k_{\perp} (the upper left corner of each of the plots in Figure 2), the kinetic fast and whistler modes have a right-handed (positive) magnetic helicity $\sigma_m \simeq 1$, while the Alfvén and ICW modes have a left-handed (negative) magnetic helicity $\sigma_m \simeq -1$. For nearly perpendicular wavevectors with $k_{\perp} \gg k_{\parallel}$ and $k_{\perp}\rho_i \gtrsim 1$, the kinetic fast and ion Bernstein modes maintain zero magnetic helicity $\sigma_m \simeq 0$, while the KAW mode develops a right-handed (positive) magnetic helicity $\sigma_m \simeq 1$. Note that the magnetic helicity σ_m has odd parity with respect to k_{\parallel} , so that modes traveling in the opposite direction with $k_{\parallel} < 0$ will have the opposite signs of the magnetic helicity σ_m . Therefore, in the case of parallel propagating modes, it is not possible using magnetic helicity alone to distinguish between whistler waves traveling up the mean magnetic field and ICWs traveling down the mean magnetic field. Suggestions to break this degeneracy using other physical characteristics are discussed in Section 5. Linear eigenfunction calculations for lightly damped kinetic slow waves with $k_{\parallel}d_i \ll 1$ (not shown) find $\sigma'_m \sim 0$, suggesting these fluctuations would not significantly contribute to *in situ* observations of magnetic helicity.

The relevance of the magnetic helicity of the linear kinetic modes to the magnetic helicity of turbulent fluctuations in the solar wind is based on the premise that, to lowest order, some properties of the turbulent fluctuations are governed by the linear response of the plasma. This concept is central to the *quasilinear premise* (Klein et al. 2012), the idea that some properties of magnetized plasma turbulence can be understood by modeling the turbulence as a collection of randomly phased, linear waves. In this picture, the nonlinear turbulent interactions serve to transfer energy from one linear wave mode to another—thus, the picture is quasilinear. Detailed arguments in support of the quasilinear premise are presented in Klein et al. (2012).

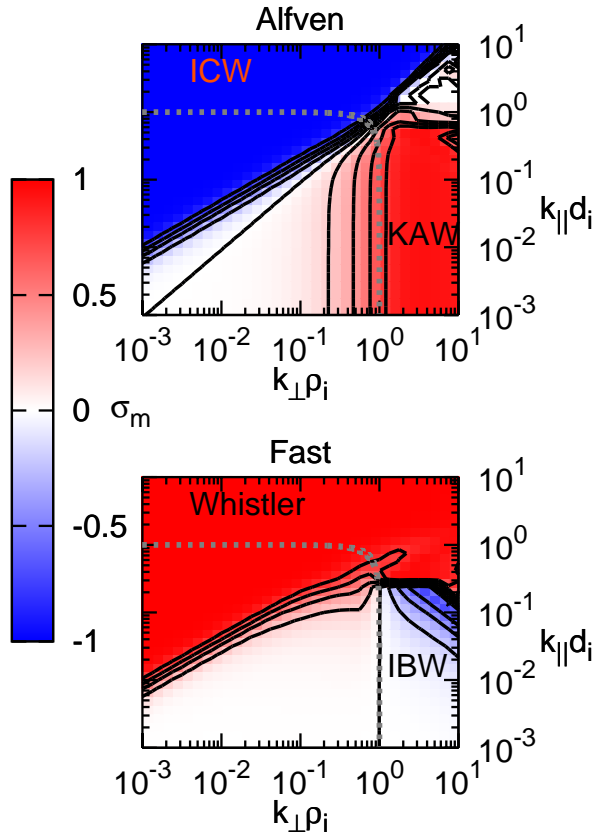


Fig. 2.— Log-log contour maps of $\sigma_m(\mathbf{k})$ for the Alfvén (top) and fast (bottom) modes as functions of $k_{\perp}\rho_i$ and $k_{\parallel}d_i$. The regions of interest for the ICW, KAW, and whistler waves are indicated. The dashed gray line demarcates $k_{\perp}\rho_i = 1$, the transition from non-dispersive to dispersive wave behavior.

Adopting the quasilinear premise, the amplitude and phase relationships among different components of a single plane-wave or mode, e.g., the three components of the magnetic field, are governed by the linear eigenfunctions of the characteristic plasma mode. The phase correlations among different plane-wave modes dictated by the nonlinear interactions, correlations that are responsible for the appearance of coherent structures and intermittency, are not described by our model.

Modern MHD turbulence theory suggests that a state of critical balance is maintained in strong plasma turbulence (Higdon 1984; Goldreich & Sridhar 1995; Boldyrev 2006), implying that the linear

terms responsible for the amplitude and phase relationships within a single plane-wave mode contribute to the evolution at the same order as the nonlinear terms responsible for the amplitude and phase relationships among different plane-wave modes. Therefore, a direct comparison of the predictions of linear wave properties of kinetic plasma physics through the synthetic spacecraft data method to *in situ* solar wind measurements can provide insight into the nature of the turbulent fluctuations present in the solar wind.

We do not directly address the possible mechanisms through which coherent structures or other nonlinear structures (Osman et al. 2012; Perri et al. 2012; Roberts et al. 2013) might produce the observed parallel and perpendicular signatures in solar wind measurements of magnetic helicity. Rather, we show that linear fluctuations arising through plausible physical mechanisms are sufficient to produce the observed magnetic helicity signatures. Further work is necessary to establish a theory through which coherent structures and other nonlinear mechanisms could replicate these magnetic helicity plots.

In this paper, we adopt the quasilinear premise and employ the synthetic spacecraft data method to generate predicted plots of the magnetic helicity σ'_m as a function of period T and angle θ . A detailed quantitative comparison of these synthetic magnetic helicity plots to observations yields stringent new constraints on the nature of turbulence in the solar wind.

3. Physically Motivated Turbulence Model

The magnetic helicity observations (He et al. 2011; Podesta & Gary 2011b) that show distinct perpendicular and parallel signatures, as described in Section 2.1 and exemplified by Figure 1, provide an important probe of the turbulence in the solar wind. Qualitatively, the perpendicular magnetic helicity signature is believed to arise from an anisotropic cascade of Alfvénic fluctuations that mediates the nonlinear transfer of energy from large to small scales (Howes & Quataert 2010; He et al. 2011; Podesta & Gary 2011b), and the parallel signature is believed to arise from fluctuations driven at ion kinetic length scales by temperature anisotropy instabilities in the spherically expanding solar wind flow (Hellinger et al. 2006; Bale et al. 2009; Podesta & Gary 2011b,a).

In this section, we present the scientific reasoning supporting this qualitative interpretation of the physics underlying the two observed magnetic helicity signatures, and then we describe a quantitative model of the turbulent fluctuations in the solar wind that we use to create synthetic magnetic helicity data for comparison to the observations.

3.1. Scientific Background for Turbulence Model

The synthetic spacecraft data method is useful in the investigation of solar wind turbulence only if a realistic model of the turbulent fluctuations can be constructed. To accomplish this goal, we exploit the significant advances in the understanding of MHD and kinetic turbulence made in the last two decades and the resulting theory of anisotropic Alfvénic turbulence (Goldreich & Sridhar 1995; Quataert 1998; Boldyrev 2006; Howes 2008; Schekochihin et al. 2009).

Accounting for the anisotropic nature of the dynamics in a magnetized plasma, Goldreich & Sridhar (1995) conjectured that strong incompressible MHD turbulence would maintain a state of critical balance, implying a preferential nonlinear transfer of energy to small perpendicular scales. This anisotropic cascade leads to small-scale fluctuations that are highly elongated along the direction of the mean magnetic field, a consequence of the wavenumber anisotropy $k_{\perp} \gg k_{\parallel}$, a condition supported by numerical simulations (Cho & Vishniac 2000; Maron & Goldreich 2001; Cho & Lazarian 2003; TenBarge & Howes 2012) and observations of turbulence in the solar wind (Horbury et al. 2008; Podesta 2009; Chen et al. 2010b; Sahraoui et al. 2010; Narita et al. 2011; Roberts et al. 2013; Podesta 2013). We refer to this anisotropic energy distribution in wavevector space as a *critically balanced distribution*.

Compressible MHD turbulence simulations demonstrate an isotropic cascade of fast waves and critically balanced distributions of Alfvén and slow waves (Cho & Lazarian 2003). Recent results using the synthetic spacecraft data method to explore the correlation between density and parallel magnetic field fluctuations have demonstrated that negligible energy exists in fast wave fluctuations in the inertial range of solar wind turbulence (Howes et al. 2012; Klein et al. 2012), so we exclude fast wave fluctuations from the inertial

range of our turbulence model.

When the Alfvénic turbulent cascade reaches the perpendicular scale of the ion (proton) Larmor radius, $k_{\perp}\rho_i \sim 1$, it has been proposed that the turbulence transitions from a cascade of MHD Alfvén waves to a cascade of kinetic Alfvén waves (Leamon et al. 1998, 1999; Howes et al. 2008b; Howes 2008; Schekochihin et al. 2009; Howes 2011), a hypothesis supported by kinetic numerical simulations of plasma turbulence (Howes et al. 2008a, 2011; TenBarge & Howes 2012, 2013; TenBarge et al. 2013) and by observations of solar wind turbulence at dissipation range scales (Sahraoui et al. 2010; Salem et al. 2012; Podesta 2013; Chen et al. 2013). Based on this wealth of theoretical, numerical, and observational evidence, the major component of the turbulent fluctuations in our model is an anisotropic Alfvénic turbulent cascade, consisting of a critically balanced distribution of Alfvén waves at scales $k_{\perp}\rho_i \ll 1$, transitioning to a critically balanced distribution of kinetic Alfvén waves at scales $k_{\perp}\rho_i \gtrsim 1$.

Observational studies have demonstrated that the temperature anisotropy, T_{\perp}/T_{\parallel} , of ion (proton) velocity distributions in the weakly collisional solar wind is bounded by the marginal stability criteria of kinetic temperature anisotropy instabilities (Kasper et al. 2002; Hellinger et al. 2006; Bale et al. 2009). In the spherically expanding solar wind flow, evolution of the temperature anisotropy can drive the plasma into an unstable regime, exciting fast-growing kinetic instabilities that tap the free energy in the anisotropic velocity distributions to drive fluctuations at characteristic kinetic scales in the plasma. We hypothesize here that *these kinetic-instability-driven waves may persist in the solar wind alongside the Alfvénic turbulent fluctuations that mediate the nonlinear transfer of energy from large to small scales*.

Specifically, for an ion temperature anisotropy $T_{\perp i}/T_{\parallel i} > 1$, the electromagnetic ion cyclotron (EMIC) instability may generate ion cyclotron waves with a rapid growth rate, $\gamma/\Omega_i \sim 1$, that peaks for parallel wavenumbers near the proton inertial length, $k_{\parallel}d_i \sim 1$. For a proton temperature anisotropy $T_{\perp i}/T_{\parallel i} < 1$, the parallel firehose instability may generate whistler waves, also with a positive growth rate, $\gamma/\Omega_i \sim 0.1$, that peaks for parallel wavenumbers near the proton inertial

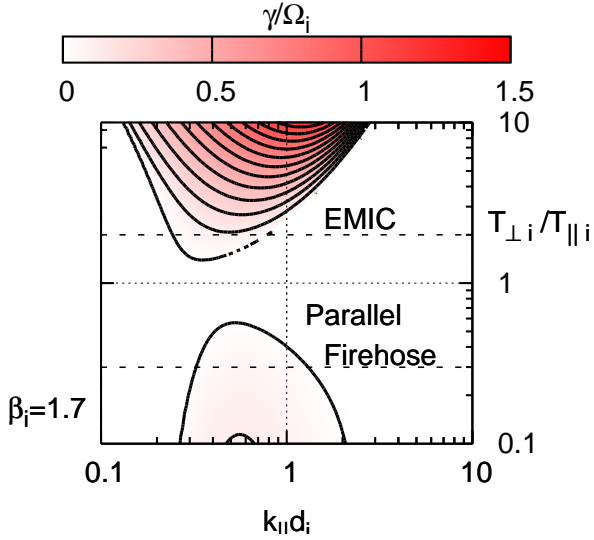


Fig. 3.— Contour map of positive growth rates γ/Ω_i parametrized by the ion temperature anisotropy $T_{\perp,i}/T_{\parallel,i}$ and the parallel scale size $k_{\parallel}d_i$ for the electromagnetic ion cyclotron (EMIC) and parallel firehose instabilities from linear kinetic theory with $k_{\perp} = 0$. We take $\beta_i = 1.7$ to match conditions for interval **I**; the resulting γ/Ω_i is similar for the parameters of the other two intervals, though the parallel firehose instability disappears for $\beta_i < 1$. The dashed horizontal lines represent approximate bounds on $T_{\perp,i}/T_{\parallel,i}$ in the solar wind near 1 AU for $\beta_i \gtrsim 1$ (Hellinger et al. 2006; Bale et al. 2009). No minority ions effects are included in this calculation, which may drastically affect the damping rates (Podesta & Gary 2011a).

length, $k_{\parallel}d_i \sim 1$. Recall that the ion cyclotron wave is the $k_{\parallel}d_i \gtrsim 1$ limit of the Alfvén wave solution to the linear Vlasov-Maxwell dispersion relation, and the whistler wave is the $k_{\parallel}d_i \gtrsim 1$ limit of the fast magnetosonic wave solution.

For plasma parameters relevant to interval **I** and assuming that unstable modes have $k_{\perp} = 0$, a contour plot of the instability growth rates for the EMIC and parallel firehose instabilities as a function of $k_{\parallel}d_i$ and $T_{\perp,i}/T_{\parallel,i}$ is presented in Figure 3, which was generated using equations (11-2) and (11-3) from Stix (1992). This plot shows that the instability growth rates are highly localized in scale to $k_{\parallel}d_i \sim 1$, suggesting that these fluctuations are generated locally, and are likely to be unrelated to the Alfvénic turbulent fluctuations

responsible for the cascade of energy from large scales. The growth rates do not drastically differ for intervals **II** and **III**, though the parallel firehose instability disappears for $\beta_i < 1$. Therefore, the secondary component of the fluctuations measured in the solar wind consists of a distribution of either ion cyclotron waves (ICWs) or whistler waves with wavevectors nearly parallel to the local mean magnetic field and $k_{\parallel}d_i \sim 1$.

As shown in Section 2.2, the normalized fluctuating magnetic helicity $\sigma_m(\mathbf{k})$ for parallel waves is $\sigma_m(\mathbf{k}) = +1$ for whistler waves and $\sigma_m(\mathbf{k}) = -1$ for ion cyclotron waves. Therefore, the parallel signature observed in spacecraft measurements with magnetic helicity $\sigma'_m \simeq -1$, as shown in Figure 1, can be explained by either ICWs propagating unidirectionally away from the sun or by whistler waves propagating unidirectionally toward the sun (Podesta & Gary 2011a). By accounting for a relative drift velocity along the magnetic field between alpha particles and protons, a characteristic frequently observed in the weakly collisional solar wind, Podesta & Gary (2011a) showed that an asymmetry may develop in the generation of unstable waves, with the result that anti-sunward ICWs are preferentially driven by the EMIC instability and that sunward whistler waves are preferentially driven by the parallel firehose instability and that the presence of an alpha particle drift can lead to an enhancement of the growth rates for both of these instabilities. Either of these instabilities would then be able to account for the observed parallel magnetic helicity signature. In addition, it has been shown that accounting for the temperature anisotropy of the alpha particles (Verscharen et al. 2013) and the presence of minor ions (Matteini et al. 2012) can significantly alter the growth rates of kinetic temperature anisotropy instabilities.

It should also be noted that an alternative interpretation of the parallel magnetic helicity signature is that it arises as part of the turbulent cascade (He et al. 2011, 2012). This viewpoint conflicts with the strong theoretical and numerical evidence discussed above that supports an anisotropic cascade with energy preferentially transferred to small perpendicular scales and little energy transferred to small parallel scales. Rather than the energy in the fluctuations responsible for the parallel magnetic helicity signature coming from nonlinear energy transfer from large scale

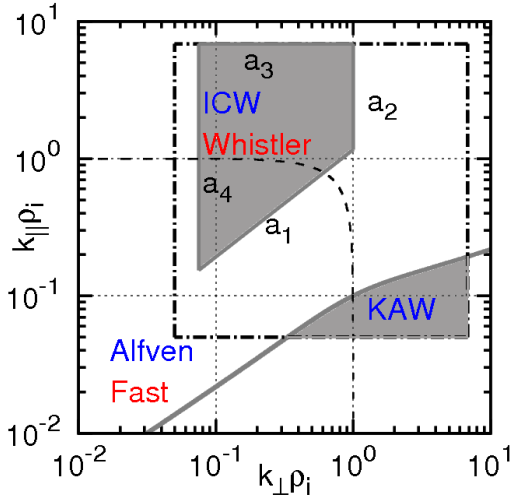


Fig. 4.— Regions of $(k_{\perp}\rho_i, k_{\parallel}\rho_i)$ parameter space in which different wave modes exist that are associated with the Alfvén (blue) and fast (red) wave solutions. The wavevector region used in creating the synthetic data is indicated by the dot-dashed box, while the limits of the perpendicular and parallel populations are indicated with solid grey lines. The perpendicular region is bounded above by the critical balance line while the parallel region is defined by four parameters a_1, a_2, a_3 and a_4 . In this study, a_1 and a_2 are kept constant and the variation of a_3 and a_4 fix the maximum and minimum values of $k_{\parallel}\rho_i$.

fluctuations through a turbulent cascade, we adhere to the viewpoint that the energy is directly injected into these parallel fluctuations at a scale $k_{\parallel}d_i \sim 1$ by kinetic instabilities (Podesta & Gary 2011b,a). Therefore, the distribution of power in parallel modes in our turbulence model is restricted to the nearly parallel wavevectors at which the instability growth rates peak, as seen in Figure 3.

3.2. Turbulence Model Parameters

As discussed above, our model for the turbulent fluctuations in the solar wind contains two main components: (i) a critically balanced distribution of Alfvén and kinetic Alfvén waves that is responsible for the perpendicular magnetic helicity signature; and (ii) a distribution of either

ion cyclotron waves (ICWs) or whistler waves with nearly parallel wavevectors peaked around a magnitude $k_{\parallel}d_i \sim 1$ that is responsible for the parallel magnetic helicity signature. A schematic diagram of the regions of wavevector space $(k_{\perp}, k_{\parallel})$ occupied by these two components is shown in Figure 4. This figure shows a logarithmic representation of the component of the wavevector perpendicular to the local mean magnetic field, $k_{\perp}\rho_i$, versus the parallel component of the wavevector $k_{\parallel}\rho_i$. Unlike in previous sections, we have chosen to normalize both the parallel and perpendicular wavevectors by the same scale length to insure a uniformly spaced grid for the creation of our synthetic spacecraft data. Wave power is assumed to be distributed axisymmetrically about the magnetic field direction in the perpendicular plane, so this two-dimensional diagram is sufficient to represent the three-dimensional distribution of power used to create our synthetic spacecraft data.

The dot-dashed box in Figure 4 indicates the perpendicular and parallel size of our synthetic plasma volume as well as the perpendicular and parallel resolution. The lower gray region (KAW) represents the portion of the critically balanced cascade of Alfvén and kinetic Alfvén waves that can be represented within the domain size and resolution limits of our synthetic plasma volume. The upper gray region (ICW or Whistler) represents the distribution of parallel wave modes populating our synthetic plasma volume. Modes with $k_{\perp} = 0$ or $k_{\parallel} = 0$ are both excluded from the synthetic volume. In addition to parameters that specify precisely the boundaries of these regions of wavevector space, our turbulence model also requires (i) two parameters that specify the imbalance of wave energy fluxes in the sunward versus anti-sunward directions for the parallel and perpendicular wave populations and (ii) one parameter that specifies the relative power between the perpendicular and parallel wave distributions. Below we define in detail each of these parameters for our turbulence model.

Power for the perpendicular distribution of Alfvén and kinetic Alfvén waves is only found in the wavevector region below the line defining critical balance (Goldreich & Sridhar 1995; Howes et al. 2008a; Howes 2011; TenBarge & Howes 2012),

$$k_{\parallel}\rho_i = (k_{\perp}\rho_i)^{1/3} \left[\frac{(k_{\perp}\rho_i)^{2/3} + (k_{\perp}\rho_i)^{7/3}}{1 + (k_{\perp}\rho_i)^2} \right], \quad (2)$$

shown by the gray line in Figure 4. This curve has a single parameter, the *isotropic driving wavenumber*, $k_0\rho_i$ (Howes et al. 2008a), which is physically determined by the outer scale of the inertial range observed in the solar wind (at the low frequencies where the measured magnetic energy frequency spectrum steepens from a spectral index of -1 to $-5/3$). For this study, we take the isotropic scale $k_0\rho_i = 10^{-3}$, a value within observationally suggested limits (Bale et al. 2005; Schekochihin et al. 2009). It is believed that this anisotropic distribution of Alfvénic fluctuations dominates the turbulent power in the solar wind, so the energy as a function of wavenumber magnitude $k\rho_i$ (assuming the Taylor hypothesis [Taylor (1938)] to convert from spacecraft-frame frequency to wavenumber) is well constrained by the magnetic energy spectrum observed in the solar wind. Therefore, *in situ* measurements of the inertial and dissipation ranges of solar wind turbulence (Sahraoui et al. 2009; Alexandrova et al. 2009; Kiyani et al. 2009; Sahraoui et al. 2010; Chen et al. 2010a; Roberts et al. 2013; Podesta 2013) lead us to specify a turbulent spectrum which scales as $k^{-5/3}$ at low wavenumbers and breaks to $k^{-2.8}$ at $k\rho_i \sim 1$. Note that using a $k^{-3/2}$ spectrum (Boldyrev 2006) instead of $k^{-5/3}$ in the inertial range has no qualitative impact on the resulting synthetic magnetic helicity measurements.

Note that the intersection of the critically balanced distribution with the parallel domain size of the synthetic plasma volume (the lower edge of the dot-dashed box in Figure 4) cuts off the representation of Alfvénic wave modes at a minimum $k_\perp\rho_i \simeq 0.3$. This lack of large scale power in the Alfvénic turbulent cascade prevents us from accurately describing the magnetic helicity signature at long periods. But, as shown in Figure 1, the dominant features of the magnetic helicity plot occur at shorter periods $T \leq 10$ s; these shorter period fluctuations are associated with the dynamics at kinetic scales $k\rho_i \sim 1$, where the intrinsic magnetic helicity $\sigma_m(\mathbf{k})$ is nonzero, as shown in Figure 2. Therefore, this limitation does not prevent this study from constraining the nature of the turbulent fluctuations at kinetic scales using the magnetic helicity as a probe.

The parallel component of the turbulence model consists of either ICWs or whistler waves distributed in the region of wavevector space with

nearly parallel wavevectors given by the upper gray region in Figure 4. The boundaries of this region are specified by four parameters: a_1 , a_2 , a_3 , and a_4 . The limits of the region in the perpendicular direction are given by $(k_\perp\rho_i)_{min} = a_4$ and $(k_\perp\rho_i)_{max} = a_2$, and the maximum in the parallel direction is given by $(k_\parallel\rho_i)_{max} = a_3$.

The lower boundary of the parallel region, associated with a_1 , is chosen to coincide with the slope of the $\sigma_m(\mathbf{k}) = -0.8$ contour in Figure 2; if the boundary is moved further down to smaller values of $k_\parallel\rho_i$, the decreasing intrinsic magnetic helicity $\sigma_m(\mathbf{k})$ from the larger scale modes reduces the resulting parallel magnetic helicity signature, preventing it from reaching the observed value $\sigma'_m \simeq -1.0$. The boundary associated with a_1 is given by the relation $k_\parallel\rho_i = a_1(k_\perp\rho_i)^{2/3}$ with $a_1 = 1.162$. The minimum parallel wavelength is therefore given by $(k_\parallel\rho_i)_{min} = a_1(k_\perp\rho_i)_{min}^{2/3} = a_1 a_4^{2/3}$. Tests have shown that, for a fixed total amount of energy in the parallel modes relative to the perpendicular modes, the magnetic helicity signature is relatively insensitive to variations in the perpendicular limits a_2 and a_4 as long as $a_2 \leq 1.0$. Unlike the perpendicular limits, the minimum and maximum parallel scale lengths are constrained by the maximum and minimum periods of the observed parallel signature from *in situ* magnetic helicity measurements, shown for instance in Figure 1. Therefore, we choose to fix the values $a_1 = 1.162$ and $a_2 = 1.0$, and allow a_3 to determine $(k_\parallel\rho_i)_{max}$ and a_4 to determine $(k_\parallel\rho_i)_{min}$. For improved clarity in describing our turbulence models, we quote the more physically relevant values of $(k_\parallel\rho_i)_{min}$ and $(k_\parallel\rho_i)_{max}$ instead of a_3 and a_4 . These parallel wavelength limits are informed by the range of $k_\parallel\rho_i$ over which the EMIC and parallel firehose instabilities arise, approximately from $k_\parallel\rho_i \in [0.2, 2.0]$, as seen in Figure 3. The precise $k_\parallel\rho_i$ boundaries used for each calculation are stated in the following section.

The energy spectrum of the parallel modes, if this component is subdominant to the anisotropic Alfvénic cascade, is not well constrained by observations. Since spectra in the direction parallel to the local mean magnetic field in the solar wind are observed to have a steeper -2 spectral index (Podesta 2009; Wicks et al. 2010; Chen et al. 2012; Horbury et al. 2012), we impose that the magnetic energy spectrum of the parallel modes is a broken power-law with k^{-2} in the inertial range,

transitioning at $k\rho_i = 1$ to $k^{-3.2}$ in the dissipation range. The dissipation range scaling for the parallel modes was chosen to match solar wind observations (Chen et al. 2010a). Minor variation of this scaling has no qualitative effect on the resulting synthetic magnetic helicity measurements.

An important physical property is that all of the waves populating our synthetic plasma volumes—including Alfvén and kinetic Alfvén waves with nearly perpendicular wavevectors, $k_\perp \gg k_\parallel$, and Alfvén, ion cyclotron, fast, and whistler waves with nearly parallel wavevectors, $k_\parallel \gg k_\perp$ —propagate with group velocities nearly exactly along the local mean magnetic field. Therefore, two important unknown parameters in our turbulence model are the parallel Poynting fluxes of electromagnetic wave energy along the local mean magnetic field for the perpendicular modes S_z^\perp and for the parallel modes S_z^\parallel . For the synthetic spacecraft data method, we define the *normalized parallel Poynting flux*, $S_z \equiv \hat{\mathbf{z}} \cdot \mathbf{E} \times \mathbf{B} / |E||B|$, where $\hat{\mathbf{z}}$ is aligned with the local mean magnetic field \mathbf{B}_0 . In MHD theory, the cross helicity σ_c is commonly used to specify this balance of upward versus downward wave energy fluxes along the mean magnetic field, but this standard definition breaks down at sub-Larmor scales, $k\rho_i \gtrsim 1$, due to the decoupling of the ion and electron fluids and the introduction of finite magnetic compressibility. Therefore, we use the more generally applicable normalized parallel Poynting flux S_z to specify the *imbalance* of upward versus downward wave energy fluxes. The values of S_z^\perp and S_z^\parallel used in our turbulence model are constant and independent of wavevector.

We denote a case with equal counterpropagating wave energy fluxes as *balanced* turbulence, and a case with unequal wave energy fluxes as *imbalanced* turbulence (Lithwick et al. 2007; Beresnyak & Lazarian 2008; Chandran 2008; Perez & Boldyrev 2009; Podesta 2009). Theoretical considerations (Podesta & Gary 2011a) suggest that the parallel modes should be close to unidirectional, $S_z^\parallel = \pm 1$, to maximize the parallel magnetic helicity signal. We do not assume a balanced or imbalanced distribution of waves *a priori*, but rather vary the power in sunward and anti-sunward waves individually for the perpendicular and parallel populations to find the best agreement with observations. We shall see that the values of S_z^\parallel and S_z^\perp in our

model are tightly constrained by comparison to the magnetic helicity observations.

The final parameter of our model is the relative power between the perpendicular and parallel populations of waves, parametrized by $P_\perp / (P_\perp + P_\parallel) = P_\perp / P_{tot}$. Since the parallel wave modes are expected to be locally concentrated around $k_\parallel\rho_i \sim 1$, whereas the perpendicular modes are part of an anisotropic turbulent cascade from large to small scales, we compare only the power in a band of wavenumbers with $k\rho_i \in [0.9, 1.1]$. We shall see that the parameter P_\perp / P_{tot} is also tightly constrained by these comparisons to the magnetic helicity observations.

In summary, the successful application of the synthetic spacecraft data method requires that a realistic model of the turbulent fluctuations can be constructed. Based on theoretical arguments, the results of direct numerical simulations, and *in situ* solar wind measurements, we have defined in this section a physically motivated model for the turbulent fluctuations. Although the turbulence model depends on a number of parameters, many of these parameters are well constrained by observations. For all of the tests presented in this study, we choose $k_0\rho_i = 10^{-3}$, $a_1 = 1.162$, and $a_2 = 1.0$. This leaves five free parameters for each turbulence model: (1) the minimum parallel wavenumber of the parallel waves, $(k_\parallel\rho_i)_{min}$; (2) the maximum parallel wavenumber of the parallel waves, $(k_\parallel\rho_i)_{max}$; (3) the imbalance of wave energy flux for the parallel waves, S_z^\parallel ; (4) the imbalance of wave energy flux for the perpendicular waves, S_z^\perp ; and, (5) the ratio of power in the perpendicular modes to the total power, P_\perp / P_{tot} . As will be demonstrated, even though this is a large number of parameters, the characteristics of the plot of magnetic helicity as a function of angle and period strongly constrain each of these parameters, yielding a valuable new approach to constrain the properties of the turbulent fluctuations in the solar wind.

4. Results of Synthetic Spacecraft Data Method

To generate a synthetic plot of the magnetic helicity as a function of angle and period to compare directly to spacecraft observations, we employ the *synthetic spacecraft data method* (Klein et al. 2012). The general technique em-

ployed to construct synthetic data, outlined in Klein et al. (2012), is briefly summarized here. In this method, first, the turbulent plasma is modeled by a three-dimensional synthetic plasma volume containing a uniform background magnetic field B_0 and a population of randomly phased linear waves with wavevector distribution defined by the turbulence model described in Section 3. The linear kinetic eigenfunctions of the wave modes are used to specify all of the fields associated with the turbulence, including the magnetic field, the electric field, plasma fluid velocity, and the density. Next, the plasma is sampled at the position of a probe moving with uniform velocity $-\mathbf{V}_{SW}$ with respect to the plasma to generate reduced time series comparable to single-point spacecraft measurements. Finally, these synthetic time series may then be analyzed with procedures identical to those used to analyze *in situ* spacecraft measurements.

4.1. Construction of Synthetic Spacecraft Data

We here focus on the resulting synthetic time series for the magnetic field using the turbulence model outlined in Section 3. For each of the three chosen solar wind intervals, defined in Table 1, we specify the synthetic plasma volume by a 256^3 grid in (k_x, k_y, k_z) space, where the local mean magnetic field \mathbf{B}_0 is aligned with the $\hat{\mathbf{z}}$ direction. To compare with the *in situ* measurements, we require a wavevector range that yields spacecraft frame periods down to $T_{min} = 1$ s, so our maximum wavevector magnitude is computed using $(k\rho_i)_{max} = 2\pi\rho_i/(T_{min}V_{SW})$. For interval **I**, $\rho_i/V_{SW} = 0.544$ s, yielding a three-dimensional wavevector grid with $0.0267 \leq k_j\rho_i \leq 3.418$, where $j = x, y, z$. The other two intervals have similarly spaced grids.

The eigenfunctions of the chosen wave modes are calculated using the linear Vlasov-Maxwell dispersion relation (Stix 1992; Quataert 1998) for each fully resolved wavevector (k_x, k_y, k_z) satisfying $|k_x|, |k_y|, |k_z| < |k_{max}|$. The value of β_i is given by Table 1, and we take $T_i/T_e = 1$ and $v_{ti}/c = 10^{-4}$. The perpendicular region in Figure 4 is populated with randomly phased Alfvén and kinetic Alfvén waves, and the parallel region is populated with a randomly phased distribution of either ICWs or whistler waves. The properties of the turbulence model are detailed in Section 3.

The synthetic plasma volume is sampled by a probe with velocity $-\mathbf{V}_{SW}$ along a trajectory with constant angle θ between \mathbf{V}_{SW} and \mathbf{B}_0 to create a single-point time series corresponding to *in situ* satellite measurements of the solar wind. For this study, we adopt Taylor’s hypothesis and therefore we need not evolve the synthetic plasma fluctuations in time. The synthetic magnetic field time series for a probe traveling along the trajectory $\mathbf{r} = \mathbf{V}_{SW}t$ is given explicitly by

$$\mathbf{B}(t_n) = \sum_m \sum_{\mathbf{k}} \mathbf{B}_m(\mathbf{k}) e^{-i[\mathbf{k} \cdot \mathbf{V}_{SW}t_n - \phi_{m,\mathbf{k}}]}, \quad (3)$$

where the index m represents the distinct contribution from the fast or Alfvén modes and \mathbf{k} indicates the contribution from each point on the synthetic plasma grid. $\phi_{m,\mathbf{k}}$ is the unique random phase assigned to each wave type for each wavevector on the grid and $\mathbf{B}_m(\mathbf{k})$ represents the complex Fourier coefficient of wave type m at point \mathbf{k} . The resulting field satisfies a reality condition $\mathbf{B}(\mathbf{k}) \exp(-i\phi_{m,\mathbf{k}}) = \mathbf{B}^*(-\mathbf{k}) \exp(+i\phi_{m,-\mathbf{k}})$. The use of $t_n = n\Delta t$ makes explicit the discrete nature of the time series. In this work, Δt is set to either 0.5 s or 1.0 s. A detailed discussion of the derivation of Equation 3 can be found in Section 3.2.2 of Klein et al. (2012).

Once the synthetic data is created, we shift the time series of magnetic field measurements into RTN coordinates, where R is anti-parallel to the probe velocity, and T and N define the plane perpendicular to R, such that $e_R \times e_T = e_N$ where e_j is the unit vector parallel to R, T, or N. Next, we calculate the magnetic helicity σ'_m :

$$\sigma'_m(f_p) = \frac{2}{|\hat{B}(f_p)|^2} \text{Im}(\hat{B}_T(f_p)\hat{B}_N^*(f_p)), \quad (4)$$

where the discrete Fourier transform \hat{B}_j is defined for frequencies $f_p = p/(n_t\Delta t)$, $p = 0, 1, \dots, n_t/2$ as

$$\hat{B}_j(f_p) = \sum_{n=0}^{n_t-1} B_j(t_n) e^{2\pi i n p / n_t}, \quad (5)$$

where j corresponds to the R, T, or N component of the magnetic field and $\mathbf{B}(t_n)$ is the synthetic magnetic time series defined in Equation 3. Values for magnetic helicity derived from Equation 4 are independent of our choice for the orientations of N and T.

The magnetic helicity σ'_m is a function of frequency f , and angle θ . The number of time steps

in each time series is $n_t = 128$. For each synthetic plasma instance the volume is sampled along 15 trajectories with evenly spaced θ ranging from 3° to 87° . This sampling is repeated for an ensemble of 128 independent runs, over which the values of $\sigma'_m(f, \theta)$ are averaged. The size of n_t is selected so that we may sample over the higher end of the frequency sampled by the observations. The ensemble approach is taken, rather than simply increasing the size of n_t , so that the new phases ϕ_{mj} for each realization of the synthetic plasma volume may stand in for the evolution of the turbulent solar wind plasma. The results are plotted as functions of $T = 1/f$ for direct comparison to the plots of magnetic helicity as a function of angle and period constructed from *in situ* measurements. It is shown in the Appendix that the magnetic helicity maps are all symmetric about $\theta = 90^\circ$. Therefore, we only need to plot σ'_m with $\theta < 90^\circ$ in our magnetic helicity maps generated from the synthetic spacecraft time series, Figures 5-8.

The plasma parameters and the slope of the magnetic power spectrum are fixed by the observational constraints, so there remain only the five free parameters of the synthetic magnetic helicity plots: $(k_{\parallel}\rho_i)_{min}$, $(k_{\parallel}\rho_i)_{max}$, S_z^{\parallel} , S_z^{\perp} , and P_{\perp}/P_{tot} . Although this is a large number of parameters, the qualitative features of the observed magnetic helicity plots are affected by variation in each of these parameters in unique ways, so it is possible to determine quite strict constraints on all of these parameters. The resulting constraints provide significant information about the nature of the underlying turbulent fluctuations in the solar wind.

4.2. Single Wave Type Tests

To gain intuition about the qualitative characteristics of the magnetic helicity plot due to the different types of waves included in the turbulence model described in Section 3, we first attempt to fit the solar wind measurements with just one type of wave: only parallel whistler waves, only parallel ICWs, and only perpendicular KAWs. The results of these tests for the plasma parameters of interval **I** are shown in Figure 5, with the following four panels: (a) only parallel whistler waves with $S_z^{\parallel} = -1.0$, (b) only parallel ICWs with $S_z^{\parallel} = 1.0$, (c) only a critically balanced distribution of Alfvén and kinetic Alfvén waves with $S_z^{\perp} = 0.7$, and (d) solar wind observations from interval **I**.

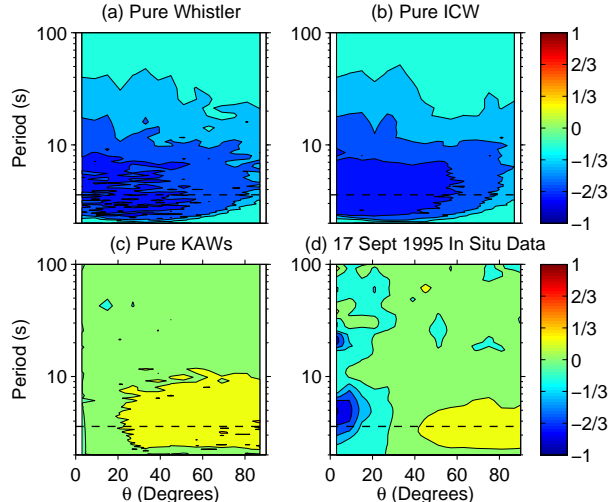


Fig. 5.— σ'_m contour maps from synthetic data sets derived using only a single mode population. None of the three solitary mode types, whistlers with $S_z^{\parallel} = -1.0$ (panel (a)), ICWs with $S_z^{\parallel} = 1.0$ (b), or KAWs with $S_z^{\perp} = 0.7$ (c), fit the interval **I** *in situ* magnetic helicity measurements (d). The correct sign for the the parallel and perpendicular populations is reproduced, but the angular extent of all three signatures are too great. The dashed black line indicates the approximate period for $k\rho_i = 1$.

For the two cases (a and b) with only parallel wave modes, the parallel signatures on the resulting magnetic helicity plots have the right sign and magnitude, but are much too extended in θ . The values of $(k_{\parallel}\rho_i)_{min} = 0.428$ and $(k_{\parallel}\rho_i)_{max} = 1.4$ used for both of these parallel wave cases do lead to a parallel signature that is limited to the appropriate range in period T .

For case (c) with only perpendicular waves, to achieve the right magnitude of the perpendicular signature, the wave energy flux cannot be unidirectional; instead, a value of $S_z^{\perp} = 0.7$ provides the best fit in magnitude. The angular extent of the perpendicular signature for this case extends down to $\theta \simeq 20^\circ$, somewhat more extended than the observed perpendicular signature in panel (d) that extends only down to $\theta \simeq 40^\circ$. The perpendicular signature is naturally limited to periods $T \lesssim 8$ s due to the fact that, for $k_{\perp}\rho_i \ll 1$, the Alfvén waves have $\sigma_m(\mathbf{k}) \simeq 0$, as shown in Figure 2. The decrease in positive magnetic helicity at $T \lesssim 3$ s

is an effect of aliasing, as will be demonstrated in Section 4.5.

In summary, these tests demonstrate that the data cannot be reproduced using only a single type of wave. A combination of both parallel and perpendicular distributions of waves is necessary to reproduce qualitatively the parallel and perpendicular signatures and to limit the extent of these signatures in angle θ and period T .

4.3. Optimized Models for Intervals I–III

In this section, we present the optimized turbulence models that lead to the best fit of the plot of magnetic helicity as a function of angle and period for the three intervals of Ulysses data described in Section 2.1. The sensitivity of the result to variations in each of the model parameters is discussed in detail in Section 4.4.

A comparison between plots of σ'_m as a function of angle θ and period T derived from observational data (left column) and from synthetic spacecraft data using either parallel ICWs (center column) or parallel whistler waves (right column) is shown in Figure 6 for the three intervals. The values yielding the best fit for each of the parameters are presented in Table 2 for models using parallel ICWs and in Table 3 for models using parallel whistler waves. An important inclusion in these tables is the range of variation of each of these values within which the fit did not degrade noticeably.

For each interval, the five adjustable parameters, P_{\perp}/P_{tot} , S_z^{\perp} , S_z^{\parallel} , $(k_{\parallel}\rho_i)_{min}$, and $(k_{\parallel}\rho_i)_{max}$, were varied to obtain the best correspondence by eye between the observed and synthetic magnetic helicity plots. The value of S_z^{\parallel} was chosen to be unidirectional, $S_z^{\parallel} = \pm 1.0$ to yield the maximum amplitude signal for the parallel signature. The values of $(k_{\parallel}\rho_i)_{min}$ and $(k_{\parallel}\rho_i)_{max}$ were chosen to match the maximum and minimum periods of the dominant parallel signature. The value of P_{\perp}/P_T was varied to match the angular extent of the perpendicular signature with the spacecraft measurements while still allowing a parallel structure with $|\sigma'_m| \geq 0.8$. The value of S_z^{\perp} was adjusted so that the amplitude of the perpendicular signature would match that of the *in situ* measurement. The correspondence between both our models, using either ICWs or whistlers as the parallel component, and the *in situ* measurements is quite good for all three intervals.

The stringent constraints on the parameters of the turbulence model, particularly the power ratio P_{\perp}/P_{tot} , provides important information about the nature of turbulence in the solar wind.

4.4. Sensitivity to Parameters

It is worthwhile demonstrating the sensitivity of the synthetic magnetic helicity plot to variations in the five adjustable parameters: P_{\perp}/P_{tot} , S_z^{\perp} , S_z^{\parallel} , $(k_{\parallel}\rho_i)_{min}$, and $(k_{\parallel}\rho_i)_{max}$. Variation in each of these parameters produces a unique effect on the σ'_m plot, allowing these five parameters to be rather strictly constrained without significant problems of degeneracy.

The variations of the five parameters in this section are performed about the best fit values for interval I for combinations of KAW and whistler waves. Qualitatively similar results are found when combining KAW and ICWs. The fiducial values for the parameters, shown in Table 3, are $P_{\perp}/P_{tot} = 0.93$, $S_z^{\perp} = 0.5$, $S_z^{\parallel} = -1.0$, $(k_{\parallel}\rho_i)_{min} = 0.43$, and $(k_{\parallel}\rho_i)_{max} = 1.4$.

The angular extent of the parallel and perpendicular signatures on the observed magnetic helicity plot strongly constrains the relative power between the parallel and perpendicular waves, P_{\perp}/P_{tot} . In the top row of Figure 7, we plot the result of variations in P_{\perp}/P_{tot} for interval I over the range $0.8 \leq P_{\perp}/P_{tot} \leq 0.98$ for a combination of parallel whistler waves and perpendicular KAWs. Similar results are obtained if one chooses ICWs instead of whistler waves for the parallel component of the turbulence model. The results in Figure 7 demonstrate that, for $P_{\perp}/P_{tot} \lesssim 0.9$, the parallel signature of σ'_m is too extended and the perpendicular signature is too limited in angular range to match the observations. For the three intervals studied here, P_{\perp}/P_{tot} varies from 0.97 to 0.92 (see Tables 2 and 3 for the best fit values and their acceptable ranges), but in all cases a majority of the total power is found in the perpendicular wave modes, with only a small fraction of the total wave energy attributed to the parallel wave modes.

The sign and amplitude of σ'_m for the perpendicular signature determines the allowable range of values for S_z^{\perp} . The sign of S_z^{\perp} is simply given by the sign of σ'_m . The amplitude of σ'_m for the perpendicular signature allows one to determine the balance of the wave energy fluxes along the local

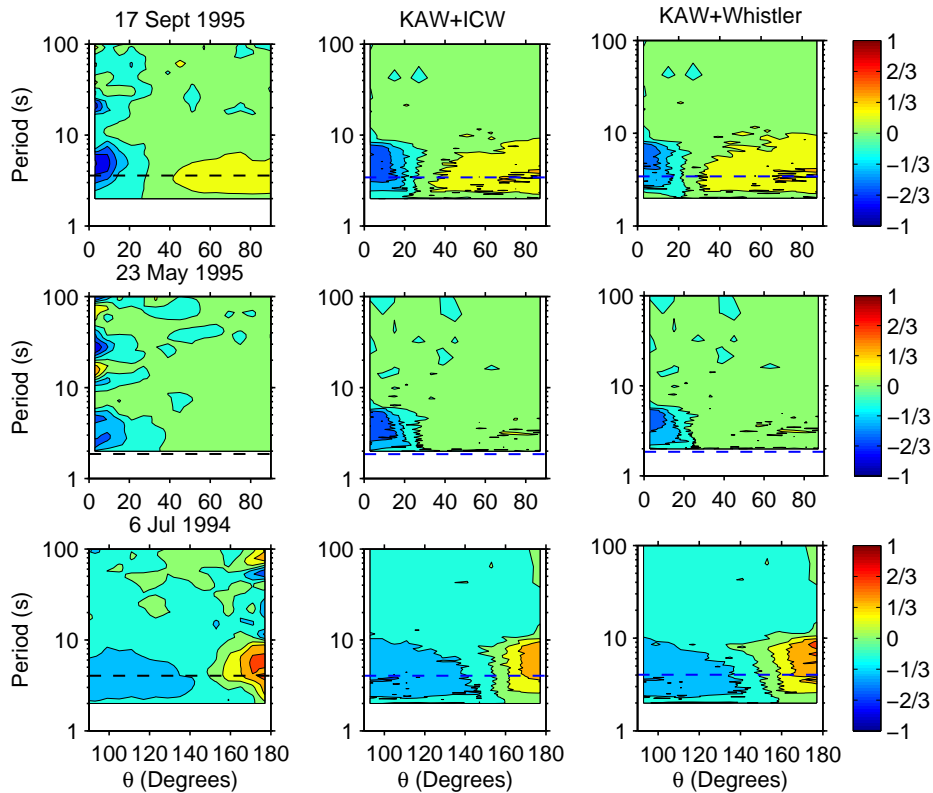


Fig. 6.— Contour plots for σ'_m from *in situ* measurements (left column), synthetic data generated with ICWs and KAWs (center column) and synthetic data generated with whistler waves and KAWs (right column). The rows correspond to the three intervals outlined in the text: **I** Sept 17 (top), **II** May 23 (middle), and **III** July 6 (bottom). Parameter values for each of these best fit models are given in Tables 2 and 3. The dashed horizontal lines indicate an approximate value for $k\rho_i = 1$.

mean magnetic field. Specifying a population of unidirectional KAWs with $|S_z^\perp| \simeq 1$ yields a magnitude of σ'_m that is too large, while for a balanced case with $|S_z^\perp| \simeq 0$, the perpendicular signature disappears. These cases are clearly demonstrated by comparing the best fit plots in Figure 6. The top and bottom rows are rather imbalanced, with $S_z^\perp = 0.7$ and $S_z^\perp = -0.6$, respectively. The middle row demonstrates a very important feature of the magnetic helicity plot. In this case, the KAW component of the turbulence is much more balanced, with $S_z^\perp = 0.2$. Although the perpendicular signature has vanished, the angular extent of parallel signature is still restricted to small θ . In the case where there is no perpendicular wave energy at all, as shown in the pure parallel cases

highlighted in Figure 5, the parallel signature extends to large angles. Therefore, the absence of a perpendicular signature in the magnetic helicity plot does not indicate the absence of a perpendicular KAW turbulent cascade, but rather a case of nearly balanced KAW turbulence.

A brief discussion in Podesta & Gary (2011b) commented on the possibility that the symmetry of the magnetic helicity signature about $\theta = 90^\circ$ observed in the solar wind could be indicative of a balanced population of KAWs. As a balanced population of KAWs would produce a magnetic helicity of zero, they suggested other mechanisms may be needed to account for the observed nonzero magnetic helicity signature near $\theta = 90^\circ$. However, the concerns raised by Podesta & Gary

Interval	KAW + ICW	P_{\perp}/P_{tot}	S_z^{\perp}	S_z^{\parallel}	$k_{\parallel}\rho_i^{min}$	$k_{\parallel}\rho_i^{max}$
I	Sept 17	$0.93^{+0.05}_{-0.05}$	$0.5^{+0.2}_{-0.2}$	$1.0^{+0.00}_{-0.25}$	$0.43^{+0.1}_{-0.1}$	$1.4^{+0.2}_{-0.2}$
II	May 23	$0.93^{+0.02}_{-0.02}$	$0.2^{+0.2}_{-0.1}$	$1.0^{+0.00}_{-0.25}$	$0.32^{+0.1}_{-0.1}$	$1.0^{+0.2}_{-0.2}$
III	July 6	$0.96^{+0.02}_{-0.05}$	$-0.6^{+0.2}_{-0.2}$	$-1.0^{+0.25}_{-0.00}$	$0.42^{+0.1}_{-0.1}$	$1.6^{+0.2}_{-0.2}$

Table 2: Table of parameters for optimized turbulence models using a combination of ICWs and KAWs for the three selected intervals.

Interval	KAW + Whistler	P_{\perp}/P_{tot}	S_z^{\perp}	S_z^{\parallel}	$k_{\parallel}\rho_i^{min}$	$k_{\parallel}\rho_i^{max}$
I	Sept 17	$0.93^{+0.05}_{-0.05}$	$0.5^{+0.2}_{-0.2}$	$-1.0^{+0.25}_{-0.00}$	$0.43^{+0.1}_{-0.1}$	$1.4^{+0.2}_{-0.2}$
II	May 23	$0.92^{+0.02}_{-0.02}$	$0.2^{+0.2}_{-0.1}$	$-1.0^{+0.25}_{-0.00}$	$0.32^{+0.1}_{-0.1}$	$1.0^{+0.2}_{-0.2}$
III	July 6	$0.97^{+0.01}_{-0.05}$	$-0.6^{+0.2}_{-0.2}$	$1.0^{+0.0}_{-0.25}$	$0.42^{+0.1}_{-0.1}$	$1.6^{+0.2}_{-0.2}$

Table 3: Table of parameters for optimized turbulence models using a combination of whistler and KAWs for the three selected intervals.

(2011b) are invalid. In the Appendix, we prove that the magnetic helicity map is symmetric about $\theta = 90^\circ$. This proof differs from the one presented by He et al. (2012). Our work with the synthetic time series shows that an imbalanced population of KAWs generates a normalized helicity signature that is symmetric about $\theta = 90^\circ$ and is consistent with solar wind observations. This minor comment by Podesta & Gary (2011b) is erroneous and we feel obliged to correct that mistake in this paper.

Analogous to the manner in which the perpendicular magnetic helicity signature diminishes as the wave energy fluxes of KAWs become more balanced, $S_z^{\perp} \rightarrow 0$, the amplitude of the parallel σ'_m signature diminishes as $|S_z^{\parallel}|$ is reduced from 1 to 0. This reduction is shown in the center row of figure 7, where S_z^{\parallel} for a population of whistler waves increases from -1 through -0.75 to -0.5 . As stated in previous studies (Podesta & Gary 2011a), the parallel component must be nearly unidirectional to match the observed amplitude of the parallel signature in σ'_m .

Finally, the region of wavevector space filled by the parallel population of waves is directly constrained by the observed minimum and maximum period of the parallel signature on the magnetic helicity plot. The maximum period T_{max} is directly controlled by our model parameter $(k_{\parallel}\rho_i)_{min}$, and the minimum period T_{min} is directly controlled by $(k_{\parallel}\rho_i)_{max}$. The observed max-

imum period of the parallel signature¹ for intervals **I–III**, as seen in the first column in Figure 6, has a range of values $6 \text{ s} < T_{max} < 10 \text{ s}$. These values are matched in the turbulence models in Figure 6—both ICW (center column) and whistler (right column) models—by setting values of the the minimum parallel wavenumber $(k_{\parallel}\rho_i)_{min} = 0.43, 0.32, 0.42$. Likewise, to see the effect of $(k_{\parallel}\rho_i)_{max}$ on the observed T_{min} of the parallel magnetic helicity signature, in the bottom row of Figure 7, we plot $(k_{\parallel}\rho_i)_{max} = 3.0, 1.4, 1$. It is clear the increasing $(k_{\parallel}\rho_i)_{max}$ has the effect of decreasing T_{min} of the parallel signature. Further discussion of the effect of aliasing on the T_{min} limit of the parallel signature for the $(k_{\parallel}\rho_i)_{max} = 3.0$ case is presented in Section 4.5.

4.5. Effects of Aliasing

A salient feature of the observed plots of magnetic helicity as a function of angle, θ , and period in the spacecraft frame, T , is that the perpendicular signature drops to zero magnetic helicity, $\sigma'_m \simeq 0$, at the shortest periods, or highest frequencies. This has previously been interpreted as indicating that the anti-sunward and sunward energy fluxes of the waves responsible for the perpendicular signature are gradually becoming more balanced at smaller scales (He et al. 2012). In stark contrast to this interpretation, we hypoth-

¹Note that we focus here on the largest peak of the parallel signature at $T < 10 \text{ s}$. The signal of this largest peak is clearly significant, but it is not clear if the smaller peaks that sometimes appear at $T > 10 \text{ s}$ are significant.

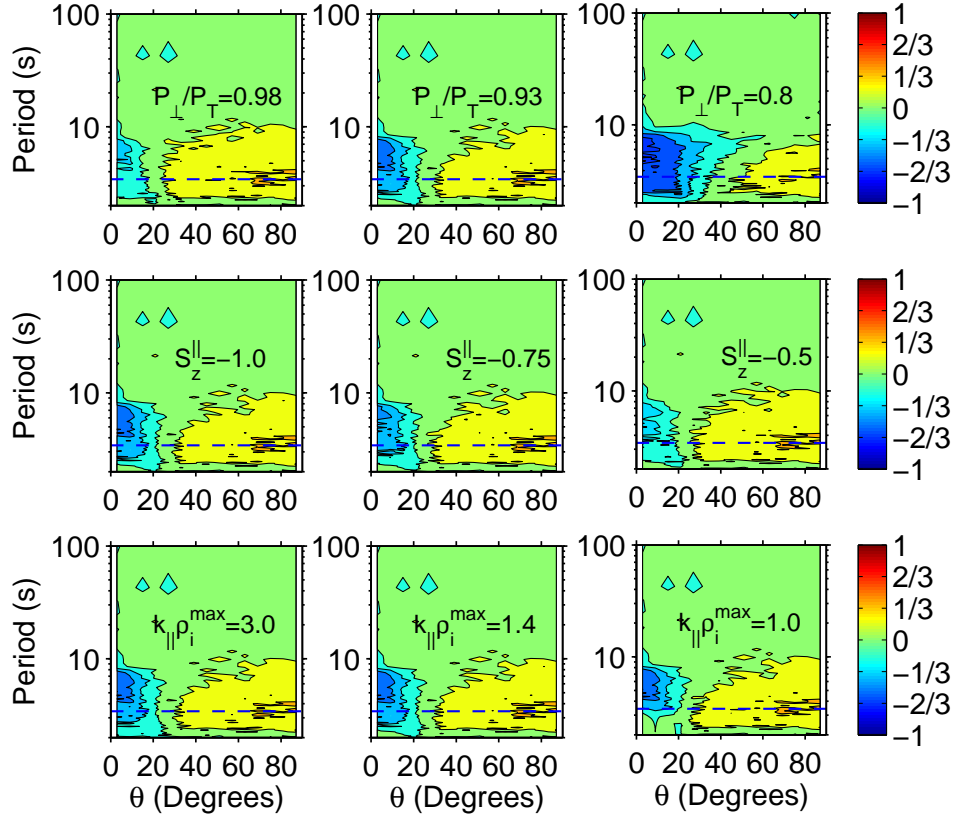


Fig. 7.— Contours of σ'_m for a variation of P_{\perp}/P_{tot} (top row), S_z^{\parallel} (center row) and $k_{\parallel}\rho_i^{max}$ (bottom row). The plasma parameters are set to mimic interval **I** conditions. All nine cases are mixtures of whistler waves and KAW; similar results (not shown) are obtained for ICW and KAW combinations. The dashed horizontal lines indicate approximate values for $k\rho_i = 1$.

esize here that the observed drop of the perpendicular signature to $\sigma'_m \simeq 0$ at the highest frequencies is simply an artifact of aliasing, and we here present evidence in support of this hypothesis.

The sampling interval for the *Ulysses* measurements presented in Figure 6 is $\Delta t = 1$ s, leading to a Nyquist frequency of $f_{Ny} = 0.5$ Hz. The turbulent magnetic field fluctuations measured in the solar wind certainly contain power at frequencies $f > f_{Ny}$, so it is inevitable that aliasing will affect the Fourier transforms of the measured magnetic field, and this may alter the determination of the magnetic helicity of the turbulent fluctuations. We explore here how such aliasing impacts the appearance of the plot of magnetic helicity as a function of angle and period.

Let us consider how aliasing impacts the magnetic helicity determination for interval **I**. Assuming the Taylor Hypothesis (Taylor 1938), the maximum frequency f_{max} of the magnetic field in our synthetic plasma volume occurs when the probe samples directly along one of the coordinate directions, $f_{max} = (k\rho_i)_{max}/(2\pi)(V_{SW}/\rho_i)$. For $(k\rho_i)_{max} = 3.418$ and $\rho_i/V_{SW} = 0.544$ s, we obtain $f_{max} = 1$ Hz. Note that since we do not sample exactly along the coordinate directions ($\theta = 0$ or $\theta = \pi/2$), the maximum frequency that we obtain is $f_{max} < 1$ Hz, avoiding the marginally aliased case when sampling at a time resolution of $\Delta t = 0.5$ s. Therefore, generating synthetic time series with a time resolution of $\Delta t = 0.5$ s is sufficient to capture completely all information in

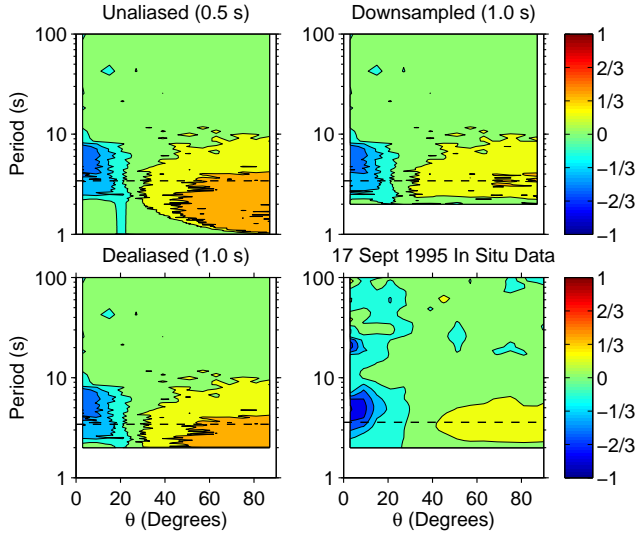


Fig. 8.— The effects of aliasing on the magnetic helicity σ'_m : unaliased signal from the $\Delta t = 0.5$ s time series (upper left), aliased signal from the downsampled $\Delta t = 1$ s time series (upper right), the dealiased signal from low-pass filtered, downsampled $\Delta t = 1$ s time series (lower left), and *Ulysses* observations from interval I (lower right).

the signal without aliasing, since the Nyquist frequency for this sampling rate is $f_{Ny} = 1$ Hz and therefore $f_{max} < f_{Ny}$. Constructing a magnetic helicity plot using these $\Delta t = 0.5$ s synthetic measurements leads to the unaliased result plotted in the upper left panel of Figure 8.

If the synthetic data is instead downsampled to a time resolution of $\Delta t = 1$ s (equivalent to simply eliminating every other data point from the $\Delta t = 0.5$ s time series), the resulting Nyquist frequency is $f_{Ny} = 0.5$ Hz, and therefore all power at frequencies $f > f_{Ny}$ will be folded back into the frequency range $f < f_{Ny}$. This aliasing is illustrated schematically in Figure 9, where the Fourier transform of an arbitrary component of the magnetic field, B_i , is plotted not as a function of frequency f , but as a function of period $T = 1/f$, to make more direct connection to the magnetic helicity plot. The Nyquist frequency $f_{Ny} = 0.5$ Hz (long dashed) therefore corresponds to a Nyquist period of $T_{Ny} = 2$ s. In this figure, the original turbulent magnetic field signal (short dashed) contains power below the Nyquist period, $T < T_{Ny}$.

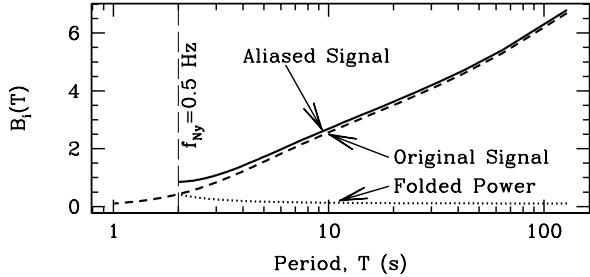


Fig. 9.— Diagram of how aliasing affects the Fourier transform of a magnetic field component, $B_i(T)$. The Nyquist frequency $f_{Ny} = 0.5$ Hz (long dashed) corresponds to a Nyquist period of $T_{Ny} = 2$ s. Power in the original signal (short dashed) at $T < T_{Ny}$ is folded back (dotted) into the measured range at $T > T_{Ny}$, leading to an aliased signal (solid) for the Fourier transform of the magnetic field component, $B_i(T)$.

This power is folded back (dotted), with a 180° phase shift, into the range $T > T_{Ny}$. This folded power combines with the original signal, leading to the aliased Fourier transform, $B_i(T)$ (solid).

Note that the scaling of the original signal as a function of period in the diagram in Figure 9 corresponds to our turbulence model as described in Section 3.2. This model yields a magnetic energy frequency spectrum that scales as $f^{-5/3}$ at $k\rho_i \ll 1$ and as $f^{-2.8}$ at $k\rho_i \gg 1$. It is important that a realistic frequency scaling is used to construct the schematic diagram in Figure 9, because the scaling of the amplitude of the signal as a function of frequency, or alternatively as a function of period, determines quantitatively how much of an impact aliasing will have on the final result.

In Figure 9, the difference between the aliased signal (solid) and the original signal (dashed) as a function of period T provides useful guidance to develop intuition about the range of T in which aliasing significantly alters the resulting signal. In this case, the difference between the original and aliased signal at the Nyquist period $T_{Ny} = 2$ s is the same magnitude as the original signal, indicating that aliasing is likely to have a large effect at this shortest measured period. The difference remains significant for periods $T \lesssim 4$ s, suggesting that aliasing will likely affect the resulting magnetic helicity plot for all periods shorter than $T \sim 4$ s, supporting our hypothesis.

We confirm the hypothesis that aliasing leads to the reduction of the magnetic helicity signal at the lowest measured periods using the synthetic data method, as shown in Figure 8. In the upper right-hand panel, the magnetic helicity is plotted for the downsampled $\Delta t = 1$ s data. Here we expect the magnetic helicity to be affected significantly by aliasing for all periods $T \lesssim 2T_{Ny} = 4$ s, as indicated schematically in Figure 9. One can clearly see in the upper right-hand panel of Figure 8 that the magnetic helicity of the perpendicular signature indeed drops to $\sigma'_m \simeq 0$ at the lowest periods, in qualitative agreement with the observed data for interval **I** plotted in the lower right-hand panel, but starkly different from the unaliased data in the upper left-hand panel.

The effect of aliasing can be eliminated if the original time series is first passed through a low-pass filter to remove all power at frequencies $f \geq f_{Ny}$ before the measurements are Fourier transformed to convert from a time series to a frequency spectrum. In this case, a low-pass filter was applied to zero out any frequencies in the range $f \geq 0.5$ Hz. This filtering was accomplished by the following procedure: (i) the $\Delta t = 0.5$ s time series is Fourier transformed to frequency; (ii) all Fourier coefficients for $f \geq 0.5$ Hz are set to zero; (iii) the resulting truncated Fourier frequency spectrum is transformed back to a time series; and (iv) the resulting $\Delta t = 0.5$ s time series is downsampled to a $\Delta t = 1$ s time series by eliminating every other data point. The magnetic helicity plot is then constructed from the resulting dealiased time series, producing the result plotted in the lower left-hand panel of Figure 8.

A comparison of the four panels plotted in Figure 8 strongly supports our hypothesis that aliasing is responsible for the drop in the magnetic helicity of the perpendicular signal at the lowest periods. The unaliased magnetic helicity plot is presented in the upper left, created by choosing a sampling time that is short enough to avoid aliasing, $\Delta t = 0.5$ s in this case. The observed magnetic helicity plot (lower right) closely resembles the aliased magnetic helicity plot (upper right) that was constructed from the downsampled $\Delta t = 1$ s time series. The dealiased magnetic helicity plot (lower left), constructed by low-pass filtering the data before downsampling, looks significantly different from the observations (lower right), but is identical to the unaliased result (up-

per left) at all periods.

This comparison strongly supports our hypothesis that aliasing significantly affects the appearance of the magnetic helicity plot at the lowest measured periods. The lesson here is that caution must be exercised not to over-interpret the apparent return of σ'_m to zero at the lowest periods.

Magnetic helicity plots generated from the *STEREO* mission, presented in Figure 4 of Podesta & Gary (2011b), further support this result. The sampling time of *STEREO A* magnetic field measurements is $\Delta t = 0.125$ s, yielding a Nyquist frequency $f_{Ny} = 4$ Hz. Although the plasma parameters for this measured interval are not significantly different from the *Ulysses* measurements presented here, the non-zero σ'_m of the perpendicular signature extends to much lower periods, $T \gtrsim 0.5$ s. In addition, the perpendicular signature of the *STEREO* measurements again drops to $\sigma'_m \simeq 0$ at $T \sim 2T_{Ny} = 0.5$ s, as our intuition about the effect of aliasing from Figure 9 suggests.

It is worthwhile noting that, for the *STEREO* measurements above, the low-period cutoff of the parallel signature is a $T \sim 1$ s, a significantly longer period than the Nyquist period, $T_{Ny} = 0.25$ s. Therefore, these measurements suggest that the parallel signature cutoff is not due to aliasing, in contrast to the case for the perpendicular signature.

5. Discussion

The magnetic helicity of the turbulent fluctuations, plotted as a function of period and angle, provides a new avenue for exploring the nature of turbulence in the solar wind. We have applied the synthetic spacecraft data method to model *in situ* magnetic helicity observations and thereby obtained new insights into the nature of the underlying plasma dynamics. Using a turbulence model inspired by the current theory for anisotropic Alfvénic turbulence and by linear kinetic plasma physics, we directly compare synthetic magnetic helicity plots to those obtained from three time intervals measured *in situ* by the *Ulysses* spacecraft. Here we explain how the findings in this study provide support for, or conflict with, the results of previous related studies.

This work is motivated by two groundbreaking observational studies of the magnetic helic-

ity of fluctuations in the solar wind. He et al. (2011) were the first to use a wavelet analysis technique to construct the magnetic helicity of the turbulent fluctuations as a function of both the period in the spacecraft frame and the angle between the solar wind flow velocity and the local mean magnetic field. This investigation used magnetic field measurements in the ecliptic from the *STEREO* spacecraft. For an outward magnetic sector, this study found a dominant negative magnetic helicity at small angles $\theta < 30^\circ$, and a broad region of dominantly positive magnetic helicity at $40^\circ < \theta < 140^\circ$. In this work, we label the narrow feature with negative magnetic helicity at $\theta < 30^\circ$ as the *parallel signature* and the broad feature with positive magnetic helicity at $40^\circ < \theta < 140^\circ$ as the *perpendicular signature*. Their interpretation was that the parallel signature arises from ICWs and that the perpendicular signature is caused by KAWs or whistler waves. They speculated that a parallel turbulent cascade of Alfvén-cyclotron waves may be responsible for the parallel signature, and that the drop to zero magnetic helicity in the dissipation range was due to the effect of pinning, in which the energy fluxes of sunward and anti-sunward waves gradually become more balanced at smaller scales.

A complementary study by Podesta & Gary (2011b) employed *Ulysses* measurements at high heliographic latitudes to obtain magnetic helicity results in accord with the earlier ecliptic observations (He et al. 2011). The interpretation of the results by Podesta & Gary (2011b), however, differed substantially from that of He et al. (2011). Podesta & Gary (2011b) suggested that the perpendicular signature was most naturally associated with the anisotropic Alfvénic turbulent cascade (Goldreich & Sridhar 1995; Leamon et al. 1999; Bale et al. 2005; Howes et al. 2008b,a; Schekochihin et al. 2009; Sahraoui et al. 2010; Howes et al. 2011; Howes 2011), consisting of Alfvén waves at MHD scales $k\rho_i \ll 1$ and KAWs at kinetic scales $k_\perp\rho_i \gtrsim 1$. In stark contrast to the interpretation of the He et al. (2011), Podesta & Gary (2011b) proposed that the parallel signature is not the result of a parallel turbulent cascade, but rather that it arises from waves driven by kinetic temperature anisotropy instabilities in the solar wind.

In a subsequent detailed study, Podesta & Gary (2011a) argued that, due to the large magnitude of

the normalized magnetic helicity associated with the parallel signature, $|\sigma'_m| \simeq 1$, the waves responsible must propagate nearly unidirectionally. For outward magnetic sectors, the negative magnetic helicity of the parallel signature could be alternatively explained either by (i) ICWs propagating away from the sun along the interplanetary magnetic field or by (ii) whistler waves propagating toward the sun along the interplanetary magnetic field. They went on to show, in the presence of a significant differential alpha-proton flow along the magnetic field $V_d \sim v_A$ (where the field-aligned drift velocity $V_d \equiv v_\alpha - v_p$), two quantitative results that could explain the observations: (i) for a temperature anisotropy of the sense $T_{p\perp}/T_{p\parallel} > 1$, the electromagnetic ion cyclotron (EMIC) instability preferentially generates anti-sunward propagating ICWs; and (ii) for a temperature anisotropy of the sense $T_{p\perp}/T_{p\parallel} < 1$, the parallel firehose instability preferentially generates sunward propagating whistler waves.

Finally, He et al. (2012) employed a simplified analytical model of the turbulent fluctuations, similar to the approach introduced by Howes & Quataert (2010), to explore whether a two-component model of parallel (slab) and perpendicular (critically balanced) Alfvénic fluctuations could explain the qualitative and quantitative features of the observed magnetic helicity plot. This model included a distribution of power in wavevector space with both a distribution of slab (parallel) ICWs and a critically balanced distribution of nearly perpendicular Alfvén waves and KAWs. In addition, the model included a prescribed “imbalance” function that defined the gradual balancing of anti-sunward and sunward Alfvén wave energy fluxes, inspired by the concept of pinning of Elsasser power spectra at the dissipation scales. Their study concluded that this two-component, slab plus critical balance model of the turbulence could qualitatively reproduce the parallel and perpendicular signatures of the observed magnetic helicity plots. In addition, with appropriate tuning of the imbalance function, the reduction of the magnetic helicity to $\sigma'_m \simeq 0$ at short periods was also reproduced by the model.

Now we turn our attention to how the method and results of the present study compare to those of these previous investigations, focusing initially on the results and interpretation of the perpendicular signature. One of the questions posed by

Podesta & Gary (2011b) was why the perpendicular signature was so broad, extending over roughly the angular range $40^\circ < \theta < 140^\circ$, even though multi-spacecraft measurements of the turbulent fluctuations at these scales (Sahraoui et al. 2010; Narita et al. 2011; Roberts et al. 2013) show fluctuations with nearly perpendicular wavevectors, $\theta = 90^\circ \pm 10^\circ$? The answer found through application of the synthetic spacecraft data method is that *the angular width of the perpendicular (and the parallel) signatures is controlled by the relative power between perpendicular and parallel wave distributions at the scales associated with spacecraft-frame periods $1 \text{ s} \lesssim T \lesssim 10 \text{ s}$* . Surprisingly, for a critically balanced distribution of Alfvén and kinetic Alfvén waves, if they are the only waves present, the perpendicular signature would extend to even smaller angles than observed, as shown in panel (c) of Figure 5. Similarly, if only a parallel distribution of whistler waves or ICWs is present, their parallel signature can extend all the way out to angles near $\theta \sim 90^\circ$, as shown by panels (a) and (b) of the same figure. The limitation of the angular range of both the perpendicular and the parallel signatures is controlled by the relative power between the perpendicular and parallel waves, as demonstrated by the top row of Figure 7.

The commonly observed transition at $\theta \sim 30^\circ$ requires that the perpendicular waves contain more than 90% of the power in the wavenumber band $0.9 \leq k\rho_i \leq 1.1$. For the three *Ulysses* intervals that we examined, we obtained values of P_\perp/P_{tot} from 92% to 97%, as presented in Tables 2 and 3. This contrasts significantly with the model used by He et al. (2012), in which the parallel component had 30% of the total power. It is worthwhile noting that, due to the statistical averaging of spacecraft measurements over long time intervals (from one to a few days), the waves responsible for the parallel signature may indeed have a much higher relative power, but be spatially intermittent, compared to the anisotropic Alfvénic turbulent cascade leading to the perpendicular signature, which is likely to be space-filling. But, in terms of the total power of magnetic field fluctuations in the solar wind, our results suggest that the parallel waves constitute on average about 5% of the power at scales near $k\rho_i = 1.0$.

The magnitude of the magnetic helicity of the perpendicular signature directly provides information about the balance of anti-sunward and sun-

ward Alfvén wave energy fluxes, parametrized by the normalized parallel Poynting flux, S_z^\perp . The synthetic spacecraft data method enables a determination of the imbalance of wave energy fluxes by adjusting parallel Poynting flux until the magnitude of the perpendicular signature from the synthetic plots matches that of the observed plots. This imbalance may vary significantly between different solar wind intervals, as demonstrated by the three *Ulysses* investigated here, which yield values for S_z^\perp of 0.5, 0.2, and -0.6 , as presented in Tables 2 and 3.

Another difference between our study and previous works is the explanation for the observed drop of the magnetic helicity of the perpendicular signature to $\sigma'_m \simeq 0$ at the shortest measured periods. He et al. (2011) and He et al. (2012) suggest that this is due to a gradual balancing of the anti-sunward and sunward wave energy fluxes, such that $|S_z^\perp|$ decreases in magnitude with decreasing length scale. We disagree with this interpretation, and show evidence that this decrease of σ'_m is merely an artifact of aliasing, as shown in Figures 8 and 9. Therefore, the observations do not necessarily imply that pinning occurs at kinetic scales. The possibility that the kinetic turbulence becomes balanced at some point in the energy cascade has not been incorporated into our model which assumes that the imbalance in the energy spectrum is scale independent.

Turning our attention to the parallel signature of the magnetic helicity plot, we present evidence in support of the idea that the waves responsible for this feature are driven by temperature anisotropy instabilities (Podesta & Gary 2011b,a), as opposed to the suggestion that a parallel turbulent cascade is responsible for these modes (He et al. 2011, 2012). In particular, when a field-aligned differential alpha-proton velocity occurs, the electromagnetic ion cyclotron (EMIC) instability can drive preferentially anti-sunward ICWs or the parallel firehose instability can drive preferentially sunward whistler waves (Podesta & Gary 2011a). The growth rate for these instabilities peaks at scales $k_\parallel d_i \sim 1$, as shown in Figure 3, so these waves are generated at the kinetic scales associated with the timescale where the parallel signature is observed and therefore, no parallel cascade is necessary. Our synthetic spacecraft data models indeed reproduce the features of the observed magnetic helicity plots

when the normalized parallel Poynting flux is unidirectional, $|S_Z^{\parallel}| \simeq 1$, and the waves are localized at parallel wavenumbers in the range $0.3 \lesssim k_{\parallel} \rho_i$. We show from a variation of our model parameters that a unidirectional, or nearly unidirectional, parallel population of waves produces a magnetic helicity plot which most closely fits with observational results; we do not assume unidirectionality based upon the theories presented in Podesta & Gary (2011a).

Although Podesta & Gary (2011a) demonstrate that anisotropy instabilities, in the presence of differential alpha-proton drift, can drive either anti-sunward ICWs or sunward whistlers, they do not attempt to distinguish between these two alternatives based on solar wind data. Here we propose several observational means to address this issue. First, the parallel firehose instability occurs only for $\beta_{p\parallel} > 1$, whereas the EMIC instability has no such restriction. Note that, due to the super-Alfvénic velocities of the solar wind, the waves measured by a spacecraft, whether they are anti-sunward or sunward propagating, will necessarily have been swept past the spacecraft in the anti-sunward direction. Therefore, the waves measured by a spacecraft must have been generated in the solar wind plasma at smaller heliocentric radius. Combining this property with the characteristic that the parallel proton plasma beta, $\beta_{p\parallel}$, in the solar wind generally increases with heliocentric radius, any waves measured in a plasma with $\beta_{p\parallel} < 1$ will almost certainly have been generated in a plasma with $\beta_{p\parallel} < 1$. Therefore, if an interval of solar wind plasma with $\beta_{p\parallel} < 1$ contains a parallel magnetic helicity signature, the parallel firehose instability cannot have been responsible for the parallel waves. In this case, one would have strong evidence that the EMIC instability is generating anti-sunward ICWs in the solar wind. One cannot, on this basis, rule out a contribution from the parallel firehose instability when $\beta_{p\parallel} > 1$.

A second way to identify which wave mode is playing a role in the parallel signature, if the waves are generated locally (in other words, the waves were generated in the same plasma volume in which they are measured), is to measure the proton temperature anisotropy of the plasma. If the temperature anisotropy is of the sense $T_{p\perp}/T_{p\parallel} > 1$, then we expect to find anti-sunward propagating ICWs caused by the EMIC instability. On the other hand, if the temperature

anisotropy is of the sense $T_{p\perp}/T_{p\parallel} < 1$, then we expect to find sunward propagating whistler waves caused by the parallel firehose instability. Studies based on measured distribution functions have shown that the EMIC instability driven by the proton temperature anisotropy is likely to operate in high speed streams (Leubner & Vinas 1986; Marsch 1991, 2006, 2012). Models of the fast solar wind relevant to the *Ulysses* measurements presented here (Hu et al. 1997; Li et al. 1999) would favor $T_{p\perp}/T_{p\parallel} < 1$, resulting from perpendicular adiabatic cooling of the protons, but direct *in situ* spacecraft measurements demonstrate that the solar wind plasma has intervals with both $T_{p\perp}/T_{p\parallel} < 1$ and $T_{p\perp}/T_{p\parallel} > 1$ (Bale et al. 2009), although in the ecliptic plane at 1 AU the condition $T_{p\perp}/T_{p\parallel} < 1$ is observed more often than $T_{p\perp}/T_{p\parallel} > 1$.

A third way to distinguish anti-sunward ICWs from sunward whistlers, if electric field measurements are available, is to use electric field measurements to compute the field-aligned Poynting flux associated with the parallel signature, S_Z^{\parallel} . The convection electric field caused by the flow of the magnetized plasma past the electric field probes (Chen et al. 2011) complicates any effort to compute the Poynting flux, but, in principle, this approach could conclusively determine which of these two wave modes is responsible. It should be mentioned that the two instabilities are not necessarily exclusive and that the solar wind magnetic helicity data is consistent with the simultaneous existence of both outward propagating ICWs and inward propagating whistlers. The three observational tests described above may prove useful in determining if either one of these instabilities is solely responsible for the quasi-parallel signature or if both instabilities play a role in its creation.

To conclude the discussion of the waves responsible for the parallel signature, we consider whether these parallel fluctuations are indeed turbulent themselves (do they transfer energy nonlinearly to small scales?), or do they merely persist in the turbulent environment caused by the anisotropic Alfvénic fluctuations responsible for the perpendicular signature. Two properties of the parallel waves argue against them driving an active turbulent cascade. First, the amplitudes of the parallel fluctuations are small (since $P_{\perp}/P_{tot} \gtrsim 0.9$), so they may not have sufficient amplitudes for strong nonlinear interactions to

occur. If the parallel waves have larger amplitude but are very intermittent, they still may not interact frequently enough for nonlinear interactions to play an important role. Second, the waves are propagating unidirectionally, and in the case of incompressible MHD, Alfvén waves traveling in one direction only do not interact nonlinearly (Howes & Nielson 2013; Nielson et al. 2013). Since the linear kinetic waves are dispersive at $k\rho_i \gtrsim 1$, however, this may enable even unidirectionally propagating waves to interact nonlinearly. The position that the parallel waves do not cascade (at least to smaller parallel scales) is consistent with the observed short period cutoff of the parallel signature, especially for the higher frequency *STEREO* measurements (He et al. 2011; Podesta & Gary 2011b). If the parallel waves are ICWs, this cutoff may be due to the efficient damping of the ion cyclotron resonance. However, if the parallel population is comprised of whistler waves, the cutoff would likely not be the result of some linear damping mechanism. This cutoff appears not to be due to aliasing, but actually represents the small parallel scale limit of the parallel waves. The hypothesis that we propose here is that the parallel waves are indeed not turbulent, but instead persist alongside the anisotropic Alfvénic turbulence. Therefore, the parallel magnetic helicity signature is a probe of a kinetic plasma physics mechanisms that operate separately from the turbulent cascade of energy from large to small scales.

6. Conclusion

Motivated by recent novel measurements of the normalized reduced fluctuating magnetic helicity in the solar wind, we undertook in this paper to illuminate the nature of the underlying turbulence through careful comparison of *in situ* and synthetic time series. The parallel and perpendicular signatures which are seen when solar wind observations of magnetic helicity are segregated by period and angle between the local mean magnetic field and solar wind velocity are replicated by synthetic time series derived from physically motivated models of turbulence. The hypothesis upon which the model is based is that the two signatures result from two distinct wavemode populations in wavevector space, namely a quasi-perpendicular collection of turbulent Alfvén/kinetic Alfvén fluctuations and a quasi-parallel collection of either

whistler or ion cyclotron waves.

In comparing the *in situ* and synthetic magnetic helicity plots, we have been able to constrain the model’s five free parameters, including the ratio of power contained in quasi-parallel versus quasi-perpendicular modes as well as the power ratio of sunward to anti-sunward modes for each of these two populations. From these comparisons, we conjecture that the parallel signature is not due to a cascade of energy to smaller parallel scales but is more likely due to a local injection of parallel energy from temperature anisotropy instabilities. These parallel modes may not be turbulent, existing along side and having little or no interaction with the cascade of energy to smaller perpendicular scales. Magnetic helicity alone is not sufficient to determine the nature of the parallel fluctuations, but we make several suggestions for a future determination of their nature. We discuss the effects of aliasing and show that the reduction of magnetic helicity amplitude to zero at small periods, which has been interpreted as evidence for an increasingly balanced turbulent cascade at smaller scales, is likely caused by aliasing and is not a physical effect. In conclusion, careful comparisons between magnetic helicity measurements and synthetic spacecraft data is capable of providing useful insight into the underlying nature of solar wind turbulence.

This work was supported by NSF CAREER AGS-1054061 and NASA NNX10AC91G. John Podesta’s contribution to this work was supported by the NSF Shine program.

A. Symmetry of the Magnetic Helicity Map about $\theta = 90^\circ$

In this appendix we show that, for angles in the range $0 \leq \theta \leq \pi$, the magnetic helicity map derived from synthetic spacecraft data is symmetric about the angle $\theta = \pi/2$. Consider a spacecraft (or observer) moving with uniform velocity $-\mathbf{V}$ along a line oriented at an angle $\theta_0 = (\pi/2) - \alpha$ with respect to the direction of the constant background field \mathbf{B}_0 , where $|\alpha| \leq \pi/2$. As described in Section 4.1, the magnetic helicity spectrum $\sigma'_m(f_p, \theta)$ is computed using Equations 4 and 5 from the magnetic field data $\mathbf{B}(t_0), \mathbf{B}(t_1), \mathbf{B}(t_2), \dots, \mathbf{B}(t_{N-1})$ taken as the spacecraft moves along that line from point \mathbf{r}_A to point \mathbf{r}_B .

Suppose, instead, that the spacecraft moves along the same line but in the opposite direction from point \mathbf{r}_B to point \mathbf{r}_A with velocity \mathbf{V} . In that case, the observations yield the magnetic helicity spectrum at an angle $\theta_1 = (\pi/2) + \alpha$. Thus, the magnetic helicity observed at the angle θ_1 is based on those same observations taken at angle θ_0 but in the reverse order: $\mathbf{B}(t_{N-1}), \mathbf{B}(t_{N-2}), \mathbf{B}(t_{N-3}), \dots, \mathbf{B}(t_0)$. The only other difference is that the system of basis vectors will be different. If $\mathbf{e}_R, \mathbf{e}_T, \mathbf{e}_N$ are the right-handed system of unit vectors employed along the trajectory from \mathbf{r}_A to point \mathbf{r}_B , then along the opposite trajectory from \mathbf{r}_B to \mathbf{r}_A we may use the right-handed system of unit vectors $-\mathbf{e}_R, \mathbf{e}_T, -\mathbf{e}_N$. Therefore, the calculation of the discrete Fourier transform $\hat{B}_j(f)$ in Equation 5 for θ_0 ,

$$\hat{B}_j(f_p, \theta_0) = \sum_{n=0}^{N-1} B_j(t_n) \exp(2\pi i p n / N), \quad (\text{A1})$$

becomes, along the opposite trajectory for θ_1 ,

$$\hat{B}_j(f_p, \theta_1) = \pm \sum_{n=0}^{N-1} B_j(t_{N-1-n}) \exp(2\pi i p n / N), \quad (\text{A2})$$

where the minus sign on the right-hand side is used for the components $j = R$ and N , and the plus sign is used for the component $j = T$. We can rewrite Equation A2 as

$$\hat{B}_j(f_p, \theta_1) = \pm \exp\{2\pi i p (N-1)/N\} \sum_{n=0}^{N-1} B_j(t_{N-1-n}) \exp\{-2\pi i p (N-1-n)/N\} \quad (\text{A3})$$

or, equivalently,

$$\hat{B}_j(f_p, \theta_1) = \pm \exp\{2\pi i p (N-1)/N\} \times [\hat{B}_j(f_p, \theta_0)]^*, \quad (\text{A4})$$

where the asterisk denotes the complex conjugate. The substitution of this expression into Equation 4 shows that

$$\sigma'_m(f_p, \theta_0) = \sigma'_m(f_p, \theta_1). \quad (\text{A5})$$

That is, the normalized magnetic helicity spectrum measured along the two directions $\theta_0 = (\pi/2) - \alpha$ and $\theta_1 = (\pi/2) + \alpha$ are equal.

REFERENCES

- Alexandrova, O., Saur, J., Lacombe, C., et al. 2009, *Phys. Rev. Lett.*, 103, 165003
- Bale, S. D., Kasper, J. C., Howes, G. G., et al. 2009, *Phys. Rev. Lett.*, 103, 211101
- Bale, S. D., Kellogg, P. J., Mozer, F. S., Horbury, T. S., & Reme, H. 2005, *Phys. Rev. Lett.*, 94, 215002
- Beresnyak, A., & Lazarian, A. 2008, *Astrophys. J.*, 682, 1070
- Boldyrev, S. 2006, *Phys. Rev. Lett.*, 96, 115002
- Chandran, B. D. G. 2008, *Astrophys. J.*, 685, 646
- Chen, C. H. K., Bale, S. D., Salem, C., & Mozer, F. S. 2011, *Astrophys. J. Lett.*, 737, L41
- Chen, C. H. K., Boldyrev, S., Xia, Q., & Perez, J. C. 2013, *Phys. Rev. Lett.*, 110, 225002
- Chen, C. H. K., Horbury, T. S., Schekochihin, A. A., et al. 2010a, *Phys. Rev. Lett.*, 104, 255002
- Chen, C. H. K., Mallet, A., Schekochihin, A. A., et al. 2012, *Astrophys. J.*, 758, 120
- Chen, C. H. K., Wicks, R. T., Horbury, T. S., & Schekochihin, A. A. 2010b, *Astrophys. J. Lett.*, 711, L79
- Cho, J., & Lazarian, A. 2003, *Mon. Not. Roy. Astron. Soc.*, 345, 325
- Cho, J., & Vishniac, E. T. 2000, *Astrophys. J.*, 539, 273
- Gary, S. P. 1986, *J. Plasma Phys.*, 35, 431
- Gary, S. P., & Winske, D. 1992, *J. Geophys. Res.*, 97, 3103
- Goldreich, P., & Sridhar, S. 1995, *Astrophys. J.*, 438, 763
- Goldstein, M. L., Roberts, D. A., & Fitch, C. A. 1994, *J. Geophys. Res.*, 99, 11519
- Hamilton, K., Smith, C. W., Vasquez, B. J., & Leamon, R. J. 2008, *Journal of Geophysical Research (Space Physics)*, 113, 1106
- He, J., Marsch, E., Tu, C., Yao, S., & Tian, H. 2011, *Astrophys. J.*, 731, 85
- He, J., Tu, C., Marsch, E., & Yao, S. 2012, *Astrophys. J.*, 749, 86
- Hellinger, P., Trávníček, P., Kasper, J. C., & Lazarus, A. J. 2006, *Geophys. Res. Lett.*, 33, 9101
- Higdon, J. C. 1984, *Astrophys. J.*, 285, 109
- Horbury, T. S., Forman, M., & Oughton, S. 2008, *Phys. Rev. Lett.*, 101, 175005
- Horbury, T. S., Wicks, R. T., & Chen, C. H. K. 2012, *ssr*, 172, 325
- Howes, G. G. 2008, *Phys. Plasmas*, 15, 055904
- . 2009, *Nonlin. Proc. Geophys.*, 16, 219
- . 2011, *Astrophys. J.*, 738, 40
- Howes, G. G., Bale, S. D., Klein, K. G., et al. 2012, *Astrophys. J. Lett.*, 753, L19
- Howes, G. G., Cowley, S. C., Dorland, W., et al. 2008a, *J. Geophys. Res.*, 113, 5103
- Howes, G. G., Dorland, W., Cowley, S. C., et al. 2008b, *Phys. Rev. Lett.*, 100, 065004
- Howes, G. G., & Nielson, K. D. 2013, *Phys. Plasmas*, 20, 072302
- Howes, G. G., & Quataert, E. 2010, *Astrophys. J. Lett.*, 709, L49
- Howes, G. G., Tenbarge, J. M., Dorland, W., et al. 2011, *Phys. Rev. Lett.*, 107, 035004
- Hu, Y. Q., Esser, R., & Habbal, S. R. 1997, *J. Geophys. Res.*, 102, 14661
- Kasper, J. C., Lazarus, A. J., & Gary, S. P. 2002, *Geophys. Res. Lett.*, 29, 170000
- Kiyani, K. H., Chapman, S. C., Khotyaintsev, Y. V., Dunlop, M. W., & Sahraoui, F. 2009, *Phys. Rev. Lett.*, 103, 075006
- Klein, K. G., Howes, G. G., TenBarge, J. M., et al. 2012, *Astrophys. J.*, 755, 159
- Lacombe, C., & Belmont, G. 1995, *Advances in Space Research*, 15, 329
- Leamon, R. J., Matthaeus, W. H., Smith, C. W., & Wong, H. K. 1998, *Astrophys. J. Lett.*, 507, L181

- Leamon, R. J., Smith, C. W., Ness, N. F., & Wong, H. K. 1999, *J. Geophys. Res.*, 104, 22331
- Leubner, M. P., & Vinas, A. F. 1986, *J. Geophys. Res.*, 91, 13366
- Li, X., Habbal, S. R., Hollweg, J. V., & Esser, R. 1999, *J. Geophys. Res.*, 104, 2521
- Lithwick, Y., Goldreich, P., & Sridhar, S. 2007, *Astrophys. J.*, 655, 269
- Maron, J., & Goldreich, P. 2001, *Astrophys. J.*, 554, 1175
- Marsch, E. 1991, *Kinetic Physics of the Solar Wind Plasma*, ed. R. Schwenn & E. Marsch, 45–133
- . 2006, *Living Rev. Solar Phys.*, 3, 1
- . 2012, *Space Sci. Rev.*, 172, 23
- Matteini, L., Hellinger, P., Landi, S., Trávníček, P. M., & Velli, M. 2012, *Space Sci. Rev.*, 172, 373
- Matthaeus, W. H., & Goldstein, M. L. 1982, *J. Geophys. Res.*, 87, 6011
- Matthaeus, W. H., Goldstein, M. L., & Smith, C. 1982, *Phys. Rev. Lett.*, 48, 1256
- Narita, Y., Gary, S. P., Saito, S., Glassmeier, K.-H., & Motschmann, U. 2011, *Geophys. Res. Lett.*, 38, 5101
- Nielson, K. D., Howes, G. G., & Dorland, W. 2013, *Phys. Plasmas*, 20, 072303
- Osman, K. T., Matthaeus, W. H., Hnat, B., & Chapman, S. C. 2012, *Phys. Rev. Lett.*, 108, 261103
- Perez, J. C., & Boldyrev, S. 2009, *Phys. Rev. Lett.*, 102, 025003
- Perri, S., Goldstein, M. L., Dorelli, J. C., & Sahraoui, F. 2012, *Phys. Rev. Lett.*, 109, 191101
- Podesta, J. J. 2009, *Astrophys. J.*, 698, 986
- . 2013, *Sol. Phys.*, 286, 529
- Podesta, J. J., & Gary, S. P. 2011a, *Astrophys. J.*, 742, 41
- . 2011b, *Astrophys. J.*, 734, 15
- Quataert, E. 1998, *Astrophys. J.*, 500, 978
- Roberts, O. W., Li, X., & Li, B. 2013, *Astrophys. J.*, 769, 58
- Sahraoui, F., Goldstein, M. L., Belmont, G., Canu, P., & Rezeau, L. 2010, *Phys. Rev. Lett.*, 105, 131101
- Sahraoui, F., Goldstein, M. L., Robert, P., & Khotyaintsev, Y. V. 2009, *Phys. Rev. Lett.*, 102, 231102
- Salem, C. S., Howes, G. G., Sundkvist, D., et al. 2012, *Astrophys. J. Lett.*, 745, L9
- Schekochihin, A. A., Cowley, S. C., Dorland, W., et al. 2009, *Astrophys. J. Supp.*, 182, 310
- Song, P., Russell, C. T., & Gary, S. P. 1994, *J. Geophys. Res.*, 99, 6011
- Stix, T. H. 1992, *Waves in plasmas*
- Taylor, G. I. 1938, *Royal Society of London Proceedings Series A*, 164, 476
- TenBarge, J. M., & Howes, G. G. 2012, *Phys. Plasmas*, 19, 055901
- . 2013, *Astrophys. J. Lett.*, 771, L27
- TenBarge, J. M., Howes, G. G., & Dorland, W. 2013, *Astrophys. J.*, in press
- Verdon, A. L., Cairns, I. H., Melrose, D. B., & Robinson, P. A. 2009, *Phys. Plasmas*, 16, 052105
- Verscharen, D., Bourouaine, S., & Chandran, B. D. G. 2013, *ArXiv e-prints*
- Wicks, R. T., Horbury, T. S., Chen, C. H. K., & Schekochihin, A. A. 2010, *Mon. Not. Roy. Astron. Soc.*, 407, L31